CHALMERS
UNIVERSITY OF TECHNOLOGY

Investigation into losses of Li-ion batteries with different design aspects

An Environmental, Economical and Performance Analysis

Master's thesis in Electrical power engineering

KRISTOFFER AXBY

DEPARTMENT OF ELECTRICAL POWER ENGINEERING
CHALMERS UNIVERSITY OF TECHNOLOGY
Gothenburg, Sweden 2022
www.chalmers.se

Master's thesis 2022

Investigation into losses of Li-ion batteries with different design aspects

An Environmental, Economical and Performance Analysis.

KRISTOFFER AXBY

CHALMERS
UNIVERSITY OF TECHNOLOGY

Department of Electrical Power Engineering
Chalmers University of Technology
Gothenburg, Sweden 2022

Investigation into losses of Li-ion batteries with different design aspects
An Environmental, Economical and Performance Analysis.
KRISTOFFER AXBY

Supervisor: Evelina Wikner, Department of Electrical Power Engineering
Examiner: Torbjörn Thiringer, Department of Electrical Power Engineering

Master's Thesis 2022
Department of Electrical Power Engineering
Chalmers University of Technology
SE-412 96 Gothenburg
Telephone +46 31 772 1000

Cover: One 18650 battery cells acquired from [39].

Typeset in LaTeX
Printed by Chalmers Reproservice
Gothenburg, Sweden 2022

Investigation into losses of Li-ion batteries with different design aspects
An Environmental, Economical and Performance Analysis.
KRISTOFFER AXBY
Department of Electrical Power Engineering
Chalmers University of Technology

Abstract

Three lithium ion battery cell chemistries were investigated in order to analyse how the thickness of the electrode affects performance, greenhouse gas (GHG) emissions and cost. The three cathode chemistries chosen were $LiNi_{0.33}Mn_{0.33}Co_{0.33}O_2$ (NMC-111), $LiNi_{0.8}Mn_{0.1}Co_{0.1}O_2$ (NMC-811) and $LiFePO_4$ (LFP) each with a graphite anode. Five cathode thicknesses were chosen for the three chemistries $35\mu m$, $50\mu m$, $66.2\mu m$, $80\mu m$, $95\mu m$. Parameters of the equivalent ciruit model were acquired through a Galvanostatic Intermittent Titration Technique (GITT) test and the power/energy density was acquired through a ragone plot. The losses of the equivalent ciruit model was analyzed in a SIMULINK model of an electric vehicle. The losses of the battery parameters were compared to the GHG emissions per km travelled and the emissions caused by manufacturing the battery pack in order to find the optimal battery from an environmental design aspect. The losses of the battery was found to be less for lower thicknesses. The cost of manufacturing each pack was compared to find the least expensive pack. The LFP showed lowest emissions during battery pack assembly, but the NMC-811 provided lower emissions during cycling. The most cost efficient battery pack was the NMC-811 battery chemistry.

Keywords: NMC-811, NMC-111, LFP, GITT, ECM, Ragone, Emissions, Cost, COMSOL, SIMULINK.

Acknowledgements

I would like to thank my supervisor Evelina Wiknér and my examinor Torbjörn Thiringer for providing helpful guidance during this time as well as the support received during this project. I would like to thank the institution of Power Engineering for the opportunity to perform my thesis for you. Lastly I would like to thank my friends and family for the support given to me during this thesis period and the entire school period.

Kristoffer Axby, Gothenburg, March 2022

Contents

1
Introduction

1.1 Background

The European union introduced in 2018 a long term goal to achieve net-zero greenhouse gas (GHG) emissions by 2050 [27]. In order to be able to reach this goal the vehicle market needs to be heavily shifted towards electrical vehicles (EV). This shift is already noticeable as several car companies declare that they only will produce EVs by a certain year i.e Volvo by 2030 and Bentley by 2030 [40] [44]. The increase of EVs in the vehicle market pushes the companies to pursue optimization of their respective EVs from an environmental perspective, performance perspective and economical perspective. In the optimization process, an important part to optimize is the battery of the vehicle as it is quite costly, heavy and is a determing factor in how fast an EV can travel as well as how far it can travel during a charge. Proper modelling of the losses for the battery is therefore crucial in the design process both from a performance perspective as well as an environmental perspective. The environmental impact analysis of the battery production is of utmost importance when considering the selection of battery for the EV. As such the battery design should be performed while taking into consideration the individual GHG emission levels of the battery components as well as the GHG emission levels of producing the entire battery pack.

There are materials that are heavily prevalent in the lithium ion battery industry which has raised concerns regarding the quantity available and whether the quantity will be sufficient to meet the sustainability goal of 2050, these two materials are Lithium and Cobalt[33]. The quantity of Lithium available is projected to be enough to supply the world up till the year 2100, however, Cobalt faces a much more time pressing issue as major deficits are project to occur as early as 2030. In 2018 the European Commission released a report on the supply and demand projection of Cobalt in a time frame from 2018 to 2030, in this report a supply deficit of 8000 tonnes was projected by 2020 and this projected supply deficit would be increased to 64 000 tonnes by 2030 [25]. Battery cost is heavily tied to material cost and as the demand for cobalt increases, the prices will increase and the harder it will be to implement EVs in the general market. Cobalt is mainly extracted in the Democratic Republic of Congo (DRC), with them supplying the world with more than 50% of the total Cobalt market. The DRC has faced heavy critique on the extraction method of Cobalt as they allegedly use child labour for the extraction process [12]. Battery technologies that require less to no Cobalt is therefore in high demand.

In this thesis 15 batteries with three cathode chemistries are simulated, each cathode chemistry has five designs with different power and energy capabilities. The three chemistries will have different percentage levels of Cobalt. The losses of the batteries under operation were analysed and compared to the the environmental impact and the economical aspect of the battery production to find an optimal choice of battery.

1.1.1 Previous work

Several studies have been performed to investigate the impact of changing the electrode thicknesses of a lithium ion cell [31][8][16]. The relation between energy density and power density based on the change of electrode thickness has been documented in order to increase the range for Electric vehicles and to further improve the energy storage capability of stationary battery applications. There is however a lack of studies documenting the efficiency of lithium ion batteries with changing electrode thickness. There is also a lack of studies relating electrode thickness to emissions of greenhouse gases. This thesis aims to solve both issues by relating the performance of battery packs to the emissions required to manufacture them and the emissions occurring during cycling of the pack.

1.2 Purpose

This thesis focus is to investigate the impact of the losses that occurs in a lithium ion battery when applying changes to the electrode thicknesses and to deduce what thickness levels are desirable from a cost and environmental perspective. The research questions for the thesis to facilitate the purpose is therefore the following:

- How does the thickness of the electrodes affect the performance of the battery?
- How does the battery design impact the sizing of the battery pack in a vehicle application?
- What is the environmental impact of the different battery packs and cell designs?
- What is the economical impact of the different battery packs and cell designs?

1.3 Scope

The performance of the lithium ion battery changes with the change of state of charge, the temperature and the state of health of the battery, however, investigation into all of these aspects would be very time consuming and thus investigation based on the state of charge will be the only aspect investigated. The temperature of the battery will be limited to room temperature and the state of health of the battery will be considered optimal. When designing the battery cell, three prominent battery chemistries will be investigated. The project will primarily be focused on the battery design of the electric vehicle and thus no in depth research will be performed on the rest of the vehicle.

2

Theory

This chapter describes the theory required for the reader to understand the concepts the thesis is treating.

2.1 Lithium Ion Battery

The lithium ion cell consists of a positive and negative electrode, a separator, electrolyte and a positive and negative current collector. A general composition of a Li-ion battery cell is presented in figure 2.1, where the external circuit is connected to the current collector to allow electrons to flow from one electrode to another. While the electrons are flowing in an external circuit, lithium ions are flowing internally in the cell which allows the electrons to recombine with a lithium ion when they have travelled from one electrode to another. The transfer of charges is handled by electrochemical reactions in the form of oxidation and reduction, also kown as the redox reaction. The oxidation reaction refers to the loss of electrons in a material while the reduction reaction refers to the gain of electrons in a material. The oxidation and reduction process can be displayed as

$$Li \rightarrow Li^{+} + e^{-} \tag{2.1}$$

$$Li^{+} + e^{-} \rightarrow Li \tag{2.2}$$

where (2.1) is the oxidation process and (2.2) is the reduction process. When a circuit is connected between the positive current collector and the negative current collector, during discharge, the oxidation process at the negative electron will start, transporting electrons from the negative electrode to the positive electrode. Meanwhile, the lithium ions that are formed from the oxidation process are transported from the negative electrode towards the positive electrode through the electrolyte and the separator. As both the electron and the lithium ion arrive at the positive electrode they will recombine in a reduction reaction to a full lithium atom. During the charging process, oxidation reaction will occur in the positive electrode, the reduction reaction occurs in the negative electrode and the flow of electrons and lithium ions will be in the opposite direction from the discharging process[13].

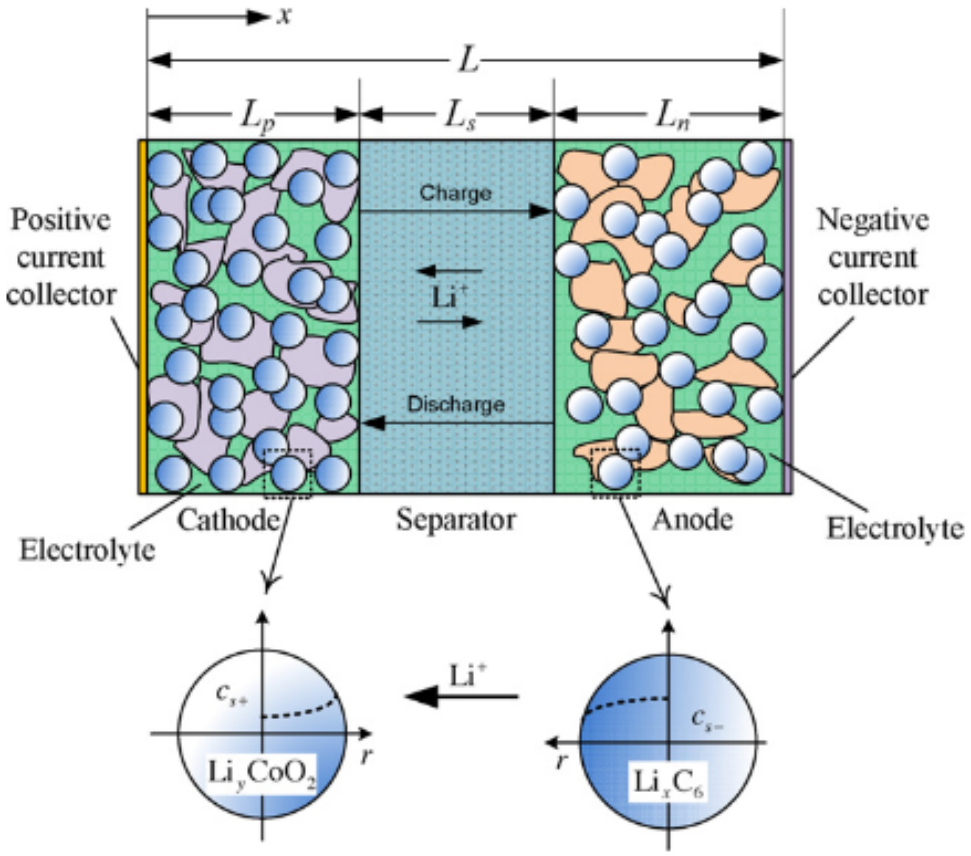

Figure 2.1: A schematic of a Lithium ion battery cell, showcasing the electrolytes ability to travel across the bulk of the electrode. Figure acquired from [6]

2.1.1 Electrolyte

The electrolyte is usually one or more salts dissolved in a solvent. The functionality of the electrolyte is that it can transport ions without being electrically conductive, providing a way to complete the transportation of ions without short circuiting the battery [13].

2.1.2 Porous Electrode

The electrode is comprised of a material that is both ionically and electrically conductive [13]. The material is layered in the form of matrices, with an electrolytic solution penetrating the void between the electrode matrices [1]. This structure, also known as a porous structure, of the electrode therefore allows for electrochemical reactions across the entire bulk of the electrode. A simplified view of the the lithium ion cell is shown in figure 2.1 to showcase the porosity of the electrode. In the lithium ion battery cell there are two electrodes, the positive electrode and the

negative electrode, also called the cathode and the anode. The positive and negative electron is named such in order to illustrate the electrochemical potential vs. lithium of the electrode. For the positive electrode it is desirable to have a high potential vs. lithium and for the negative electrode it is desirable to have low potential vs. Lithium to facilitate a high voltage between the positive and negative electrode. Besides the appropriate potential vs. lithium of the individual electrodes, desirable qualities for electrodes are also high capacity, high coulombic efficiency and acceptable ionic and electronic conductivity [13]. Figure 2.2 shows a mapping of several common positive and negative electrode materials with respect to capacity and electrochemical potential.

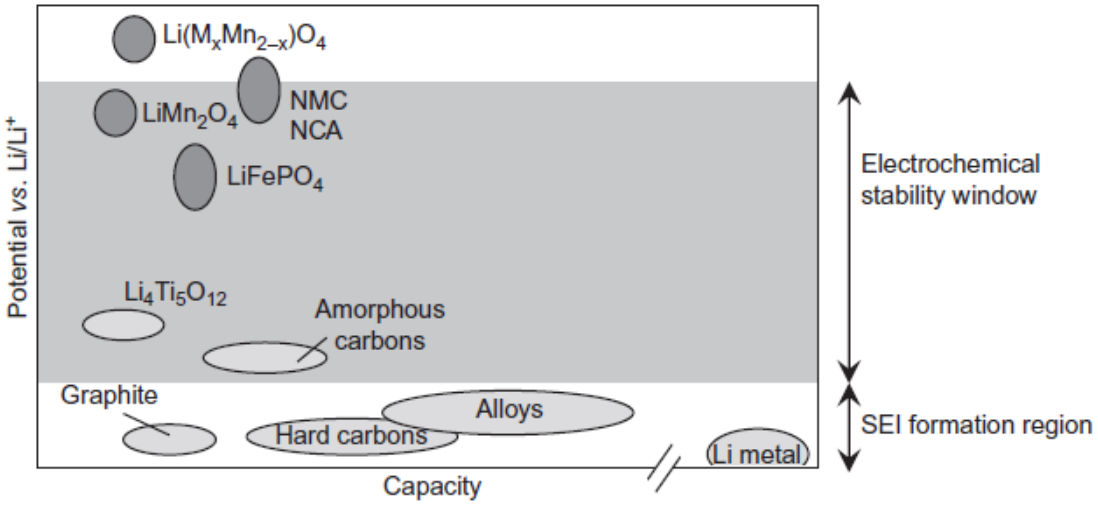

Figure 2.2: Map of capacity and potential properties of different electrode materials, picture taken from [13]

2.1.3 Separator

In order to ensure that no short circuiting will occur in the battery cell a separator is placed between the two electrodes. The material is usually a membrane which allows for high ionic conductivity. The membrane stops the two electrodes from touching each other and thus preventing short circuit while allowing the electrolyte to transport ions through it[13].

2.1.4 current collector

The positive and negative electrode are connected to current collectors on each side of the cell. These current collectors consists of highly conductive materials and their purpose are to ensure an optimal electron transportation to the outer circuit. The

positive current collector, will for this thesis, be made of aluminum and the negative current collector will be made of copper[13].

2.1.5 SEI-layer

Figure 2.2 shows the relationship between different electrode potential vs. Li/Li+, in this figure the electrochemical stability window and the SEI formation region are mentioned. The electrode materials that are in this region has the potential to form a Solid Electrolyte Interphase (SEI) - layer, which is an irreversible protective layer formed from decomposition products of the electrolyte [13]. This layer must be present across the entire surface of the anode or further decomposition of the electrolyte will occur and is first formed during the initial charging process during the battery assembly process. The decomposition of the electrolyte consumes lithium ions and for the formation of the first SEI-layer about 10 % of the original capacity is consumed [17]. Besides providing protection of further decomposition, the SEI layer also creates additional ionic and electric resistance for the battery which is presented as R_{film}. The growth of the SEI layer consumes lithium and thus lowers the capacity of the battery cell. This growth will occur during repeated charges and discharges of the battery and is what is commonly refered to as battery ageing. The limitation set on this thesis is such that the ageing of the battery will not be investigated and therefore the value of R_{film} will be set as a constant value, which is the value of the film resistance when the first formation of the SEI-layer has formed.

2.1.6 The 18650 cell

The cell design used in this thesis is that of an 18650 cell. The 18650 is a cylindrical battery cell with the dimensions of $18mm$ in diameter and $65mm$ in length and it is built using the Jelly roll design [30].

The jelly roll is constructed by layering the cell materials on top of each other and then roll the layers up into a roll. The first layer is a current collector, which is then evenly coated with the appropriate electrode material. The next layer is the separator which is followed by the opposite electrode material which in turn is followed by the appropriate current collector. In order to maximize the amount of active material in the cell, this current collector in turn is coated with its appropriate electrode slurry on the opposite side. This layer is then covered by a separator and finally the electrode appropriate to the first current collector is introduced atop the separator. Two tabs are introduced on opposite sides of the current collector sheets, one connected to the positive current collector and the other one connected to the negative which will serve as the connecting points for the external circuit. The electrolyte is introduced between the two electrodes, the layers described are then rolled up around a thin cylinder into a roll. The battery thus has a surface area equal to the area of the current collector sheet. The Jelly roll is then placed into a steel case with the positive tab representing the connecting point for the cathode and the negative tab representing the connecting point for the anode [9]. In order to ensure that the cell fits the case, calculations measuring the length of the current

collector has to be performed, these will be performed with the use of an Archimedes spiral. The layout of an Archimedes spiral is displayed in figure 2.3.

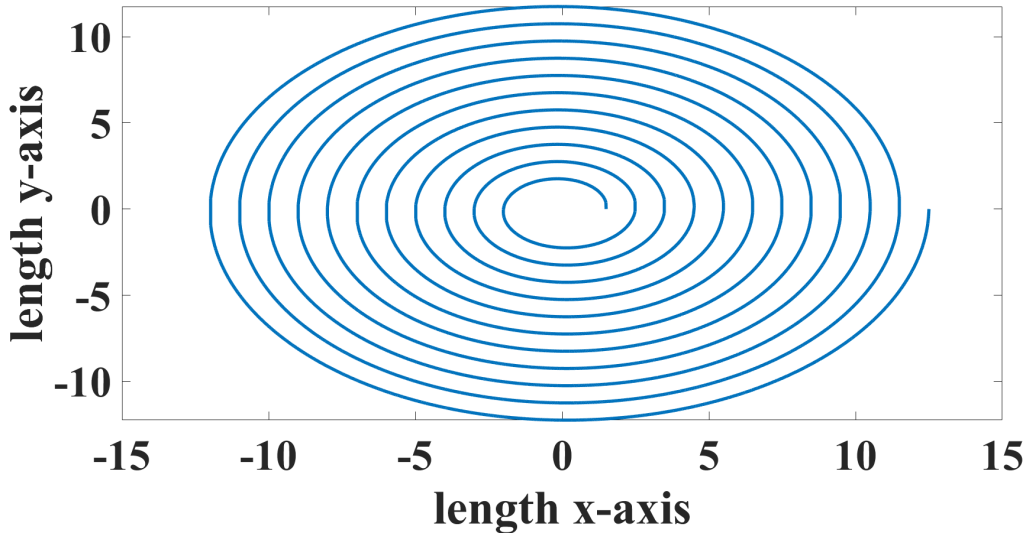

Figure 2.3: Layout of an Archimedian Spiral.

The Archimedes spiral is modelled after

$$r = a + b\theta \tag{2.3}$$

where, r is the outer radius of the spiral, a is the inner radius of the spiral, b is the distance between each layer of the spiral and θ is the angle of the rotation. For the battery cell, b will be the thickness of the jelly roll layer, a will be the radius of the cylinder the jelly roll is rolled around and will be $1mm$ for this thesis based on the data acquired from [34]. The length component of the jelly roll will be acquired through integration of the jelly roll acquired to

$$L = \int_a^{r_{max}} \sqrt{r^2 + \frac{dr}{d\theta}}\, d\theta \tag{2.4}$$

where, r_{max} is the outer radius value of the jelly roll.

2.1.7 Battery model

The dimensions of a Lithium ion cell is such that the thickness of the electrode is several degrees of magnitude lower than the surface area of the electrode, thus the electrode can be approximated to a 1-D model, with the model oriented along the axis corresponding to the axis of the thickness of the electrode. The model assumes a uniform current distribution along the bulk of the cell and as such the current in

this model is replaced with a current density corresponding to the cross section area of the battery cell [15].

2.1.7.1 Voltage calculation

The driving force behind the redox reaction is the built up energy during open circuit between the positive and negative electrode potential when no reactions are occuring. This energy is commonly called Gibbs Free Energy ΔG_{gibbs} and a change of this energy during a closed circuit will be expressed as

$$\Delta G_{cell} = -nFE_{cell} \tag{2.5}$$

where, n is expressing the number of electrons involved in reaction, F is Faraday's constant which is $96,485 As/mol$ and E_{cell} is the potential difference between the positive and negative electrode [13]. During the reaction process of the cell, the change of the free energy can be described as the difference between the sum of free energy of the products and the sum of free energy of the reactants as shown in

$$\Delta G_{cell} = \sum \Delta G_{prod} - \Delta \sum G_{react} \tag{2.6}$$

where, $\sum \Delta G_{prod}$ is free energy of the products and $\sum G_{react}$ is the free energy of the reactants. If ΔG_{cell} is positive, the energy of the products is higher than the reactants and thus no more natural flow of electricity can occur. An external source will have to be inserted with a voltage value of $E_{cell} < 0$ to force electron flow in opposite direction which will result in charging of the battery cell [13]. In equation2.6, the free energy of the products and the reactants can be represented with the electrochemical potential $\overline{\mu_i}$ of the individual species i according to

$$\Delta G_{cell} = \sum \Delta \overline{\mu}_{prod} - \Delta \sum \overline{\mu}_{react} \tag{2.7}$$

The electrochemical potential is expressed in the form of the chemical potential (μ_i) of species and the electrostatic potential difference between the electrode and electrolyte $\Delta\phi$ [13]. The chemical potential is influenced by the activity (a_i) of the species i and can be expressed as

$$\mu_i = \mu_i^0 + RTln(a_i) \tag{2.8}$$

where T (K) is the temperature in Kelvin, R is the gas constant and μ_i^0 is the standard chemical potential of species i. The electrochemical potential has to consider the electrostatic potential for species i, and is thus added to the chemical potential according to

$$\overline{\mu}_i = \mu_i^0 + RTln(a_i) + nF\phi_i \tag{2.9}$$

where ϕ_i is the electrostatic potential for each phase for species i [13]. Equation (2.9) applied to both electrodes gives a relation shown as

$$\Delta\overline{\mu}_i = \overline{\mu}_{i,+} - \overline{\mu}_{i,-} = RTln(\frac{a_{i,+}}{a_{i,-}}) + nF(\phi_{i,+} - \phi_{i,-}) \tag{2.10}$$

Combining (2.10) with (2.5) and (2.7) an expression for the cell voltage E_{cell}, known as the Nernst equation is acquired. The Nernst equation is presented as

$$E_{cell} = E^0 - \frac{RT}{nF}(\frac{a_+}{a_-}) \tag{2.11}$$

where E^0 is the resulting voltage from the electrostatic potential [13][7].

2.1.7.2 Mass transport

The transport of ions in the cell is mainly contributed to flux through diffusion (N_d) and migration (N_m) mechanisms, however, some is also contributed to convection (N_c) [13]. The diffusion is dependant on the concentration gradient of the species i, the migration is dependant on the potential gradient of the cell and convection is driven by movement of the electrolyte fluid [24]. The diffusion, migration and convection are all assumed to work independently and therefore the total flux of ions (N_T) can be explained according to

$$N_T = N_d + N_m + N_c \tag{2.12}$$

$$N_T = -D_i \nabla c_i - z_i u_i F c_i \nabla \phi + c_i v \tag{2.13}$$

Here, c_i is the concentration of species i, D_i is the diffusion coefficient, v is the velocity of the electrolyte, u_i is the ionic mobility, z_i the ionic charge, F is the Faraday constant and ϕ is the potential. As ions are transported away from the surface of the electrode, the diffusion will stop contributing to the mass transport since the concentration gradient is not present in the electrolyte phase [24]. The transport in electrolyte, according to concentrated solution theory, is driven by the gradient of electrochemical potential in addition to the migration and convection already present [3][2]. The electrolyte transport is modelled as

$$c_i \nabla \overline{\mu}_i = \sum_{i \neq j} K_{i,j}(v_j - v_i) \tag{2.14}$$

where, $\overline{\mu}_i$ is the electrochemical potential, $K_{i,j}$ is the friction coefficient for species i and j. In a binary salt solution plus solvent, there are two different independent transport equations according to the Gibbs-Duhem equation, which forces a constraint on the system at equilibrium as presented as

$$\sum_i n_i d\overline{\mu}_i = 0 \tag{2.15}$$

[3][2]. For the two independent equations based on (2.14), if the solvent is used as a reference species and the velocity is set to zero the equations can be inverted. This phenomena is presented in

$$N_+ = -\nu_+ D \nabla c + \frac{\mathbf{i} t_+^0}{z_+ F} \tag{2.16}$$

and

$$N_- = -\nu_- D\nabla c + \frac{\mathbf{i}t_-^0}{z_- F} \tag{2.17}$$

where N_+ and N_- are the flux of ions for the first and second equation, D, t_+^0 and t_-^0 are transport properties related to $K_{i,j}$, $\mathbf{i}$ are the current density, z_+ and z_- is the charge of the system, $\nu+$ and ν is the number of ions formed when 1 mol of electrolyte dissolves and finally ∇c are the gradient of the lithium salt electrolyte where $c = \frac{c_i}{\nu_i}$ [24] [3] [2] [5].

2.1.7.3 Current flow

The current flows in both the electrolyte phase and the electrode phase, however, the flow equation is different depending on which phase the current is flowing through. In the electrode phase, the current is flowing according to Ohm's Law as displayed in

$$i_s = -\sigma_s \nabla \phi_s \tag{2.18}$$

where σ_s is the conductivity of the electrode, $\nabla\phi_s$ is the gradient of the potential for the electrode and i_s is the current density of the electrode. The current in the electrolyte phase is presented as

$$i_l = -\kappa\nabla\phi_l + \frac{\kappa RT}{F}(1 + \frac{\partial ln(f)}{\partial ln(c_l)})(1 - t_+)\nabla c_l \tag{2.19}$$

where, i_l is the current density of the electrolyte, κ is the electrolyte conductivity, $\nabla\phi_l$ is the gradient of the electrolyte potential, R is the gas constant, T is the temperature, F is the Faraday constant, f is the salt activity and c_l is the lithium salt electrolyte concentration [3] [2]. In the area where the current flows from the electrolyte to the electrode and vice versa, intercalation and deintercalation occurs, where intercalation is when the lithium ions are reduced back into the electrode and deintercalation is when lithium ions are oxidised away from the electrode. The flow of current in this region is described by the Butler-Volmer equation as described in

$$i_{se} = i_0(exp(\frac{\alpha_a F}{RT}\eta) - exp(-\frac{\alpha_c F}{RT}\eta)) \tag{2.20}$$

where,

$$i_0 = F(k_c)^{\alpha_a}(k_a)^{\alpha_c}(c_{s,max} - c_s)^{\alpha_a}(c_s)^{\alpha_c} \tag{2.21}$$

and

$$\eta = \phi_s - \phi_l - U_0 \tag{2.22}$$

Here, i_{se} is the current density for the intercalation and deintercalation, α_a and α_c are the anodic and cathodic transfer coefficient, i_0 is the exchange current density, which is calculated through (2.21) and η is the overpotential calculated through (2.22). The exchange current density is dependent on the reaction rate of the anode and cathode k_a and k_c as well as the concentration c_s and the maximum concentration available

to be stored in the electrode. The overpotential is the potential difference between the electrode potential ϕ_s, electrolyte potential ϕ_l and the half cell potential U_0 [3] [2].

2.2 Electrode thickness

The thickness of the electrode decides the amount of lithium available in the electrode and as such contributes heavily to the energy density of the cell. High energy density is desirable in EVs as it directly translates to the distance the vehicle can travel, however, there are certain drawbacks which occurs for a thick electrode which will be described in this section [8].

The discharge and charge of a battery cell are determined in C-rates which are the current required to fully discharge or charge the cell during a certain time frame, $1C$ is the current required to charge/discharge the battery in 1 hour while $2C$ is for 30 min and $0.5C$ is for 2 hours. For low C-rates the characteristic diffusion length is higher than the length of the electrode and as such the energy available in the cell can be transferred properly, however, as the C-rate increases the characteristic diffusion length decreases. The energy density of the cell is slowly decreasing as the characteristic diffusion length decreases until the characteristic diffusion length becomes equal to the electrode length. After reaching this critical C-rate, any additional increase of the C-rate will cause dramatic energy density losses due to the diffusion no longer being able to operate over the entire electrode. A higher C-rate implies a higher power density of the electrode and as such a compromise between the energy density and power density has to be made, where the optimal power and energy density values occur when the characteristic diffusion length equals the electrode length [8].

When designing a cell a choice can be made of whether the cell should be power optimized or energy optimized, if the thickness of the cell is big, the energy density is high but the C-rate required for the characteristic diffusion length to reach the electrode length is low. On the other hand, a cell with a small thickness won't be able to have as high energy density but the C-rate required for the characteristic diffusion length to reach the electrode length is higher and therefore a higher power density is available [8].

2.2.1 Energy and Power Density

The power and energy density relationship of a battery cell can be displayed in the form of a Ragone plot. The ragone plot is acquired by discharging or charging the cell multiple times with different C-rates and then to display the power and energy density according to

$$W_C = \int_0^{t_{end}} \frac{i_C E_{cell}(t) A_{jelly}}{3600m} dt \tag{2.23}$$

$$P_C = \frac{W_C 3600}{t_{end}} \tag{2.24}$$

where, W_C (Wh) is the energy density of the battery for a given C-rate. $t_{end}(s)$ is the time required for a full discharge of the cell for a given C-rate. $i_C(A/m^2)$ is the current density of the 1-D model corresponding to a given C-rate and $E_{cell}(t)$ is the voltage of the cell during discharge at the given C-rate. $A_{jelly}(m^2)$ is the area of the electrode surface, since the 1-D model assumes uniform current distribution across the surface of the electrodes the area of the electrode can be assumed to be equal to the surface area of the jelly roll. $m(kg)$ is the mass of the cell, $P_C(W)$ is the power corresponding to the same C-rate as W_C and the constant 3600 is to convert units between hours and seconds.

The ragone plot is usually expressed in volumetric or gravimetric energy and power density, and as the thesis involves the power consumption of a vehicle, the weight of the battery pack is of great importance and therefore the power and energy density will be gravimetric. The weight calculation for the gravimetric power and energy density will be displayed in

$$m = m_{jelly-roll} + m_{case} \tag{2.25}$$

where,

$$m_{case} = \rho_{steel} * (pi * r_{case}^2 * H_{case} - pi * (r_{case} - t_{case})^2 * (H_{case} - t_{case})) \tag{2.26}$$

and

$$\begin{aligned} m_{jelly-roll} = {} & W_{jelly-roll} * H_{jelly-roll} * (L_{pos} * (\epsilon_{s,pos} * \rho_{cath} + \epsilon_{l,pos} * \rho_l) \\ & + L_{sep}(\epsilon_{l,sep} * \rho_l + rho_{sep}) \\ & + L_{neg}(\epsilon_{s,neg} * rho_{ano} + \epsilon_{l,neg} * rho_l) \\ & + t_{al} * rho_{al} + t_{cu} * rho_{cu} + t_{sep} * rho_{sep}) \end{aligned} \tag{2.27}$$

$r_{case}(m)$, $t_{case}(m)$ and $H_{case}(m)$ are the radius, thickness and height for the case of the battery. $W_{jelly-roll}(m)$ and $H_{jelly-roll}(m)$ are the width and height for the jelly, these two parameters are equal to the width and height of the current collectors. $L_{pos}(m)$ is the thickness of the positive electrode, $L_{neg}(m)$ is the thickness of the negative electrode and $L_{sep}(m)$ is the thickness of the separator. $\epsilon_{s,pos}$ is the volume fraction of the positive electrode, $\epsilon_{s,neg}$ is the volume fraction of the negative electrode, $\epsilon_{l,sep}$, $\epsilon_{l,neg}$ and $\epsilon_{l,pos}$ are the electrode volume fractions for the positive electrode, separator and negative electrode separately. $rho_{cath}(kg/m^3)$ and $rho_{ano}(kg/m^3)$ are the density of the positive electrode and negative electrode separately, ρ_l is the density for the electrolyte and rho_{sep} is the density for the separator. Finally ρ_{al} and t_{al} are the density and thickness of the aluminum current collector while rho_{cu} and t_{cu} are the density and thickness of the copper current collector.

2.3 Battery chemistries

For this thesis three different battery chemistries are analysed and compared, this section briefly covers each battery and its behaviour. The main anode chemistry used in the battery industry today is graphite (Li_xC_6) due to its high capacity at $350mAh/g$ and will therefore be used as anode material for all simulations performed in this thesis[13]. The potential behaviour of the Graphite is showcased in figure 2.4, where an increase in concentration of the anode are refers to an increase of State-of-charge (SOC) of the cell.

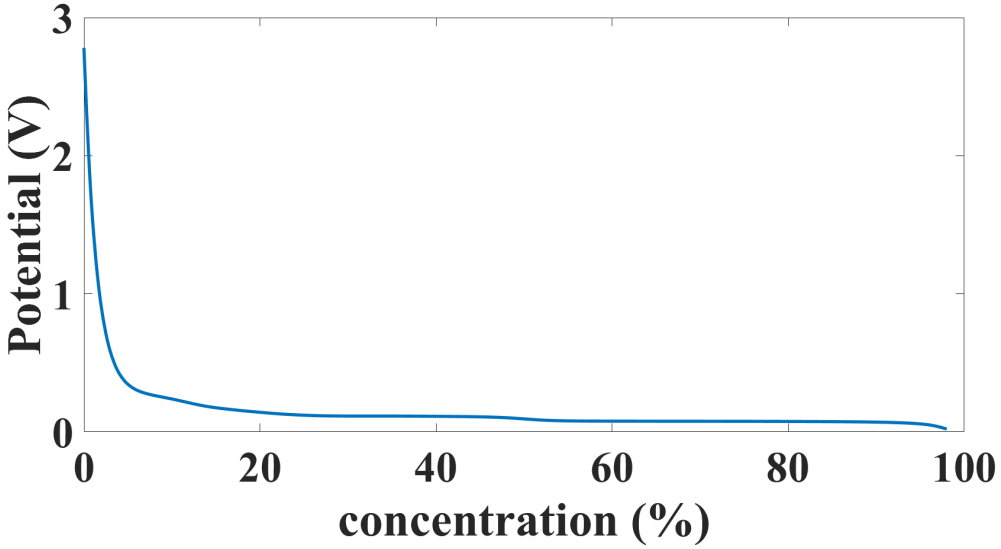

Figure 2.4: The potential versus concentration (%) of Lithium of Graphite.

2.3.1 NMC-111

$LiNi_{0.33}Mn_{0.33}Co_{0.33}O_2(NMC-111)$ is the first cathode material investigated and is called such due to the ratio of Nickel $Ni(33\%)$ to Manganese $Mn(33\%)$ and Cobalt $Co(33\%)$. The NMC chemistry is one of the main cathode chemistries used in the automotive industry today as it provides high power and energy density compared to other commercial batteries [8]. The potential behaviour depending on the capacity of the NMC-111 cathode can be viewed in figure 2.5 where the increase of capacity for a cathode refers to a discharge of the cell and a loss of SOC. The NMC chemistry has a theoretical capacity of $275mAh/g$, however in practice only $163mAh/g$ can be acquired. The structure of the NMC chemistry collapses at the higher voltage levels, and since the potential of the electrode is tied to the concentration of lithium in it, the full capacity cannot be acquired [13].

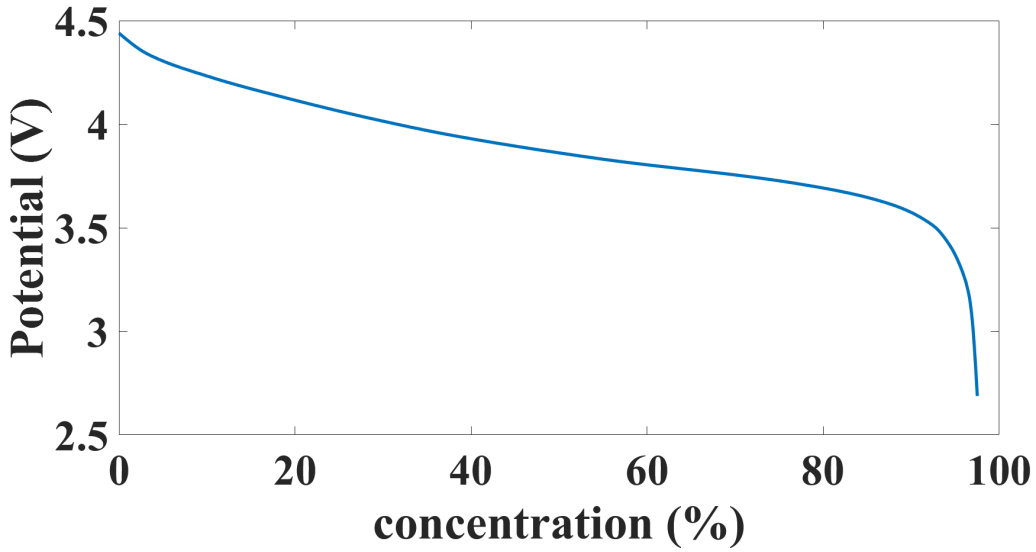

Figure 2.5: The potential versus concentration (%) of Lithium of NMC-111.

2.3.2 NMC-811

In an effort to increase the capacity of the NMC electrode, the ratios of the NMC materials has been experimented on to increase the percentage of nickel content in the electrode which also contributes to a percentage loss of Manganese and Cobalt. The furthest iteration of this effort so far has culminated in the NMC-811 cathode ($LiNi_{0.8}Mn_{0.1}Co_{0.1}O_2$) with a ratio of Nickel $Ni(80\%)$ to Manganese $Mn(10\%)$ and Cobalt $Co(10\%)$. The increase of Nickel in the electrode provides an increase to the usable capacity of the cell from $163mAh/g$ to $203mAh/g$ for NMC-111 to NMC-811 respectively, however, this comes with a lower capacity retention and higher GHG emission levels. The potential behaviour in relation to concentration of lithium (%) of the electrode is displayed in figure 2.6[22][41].

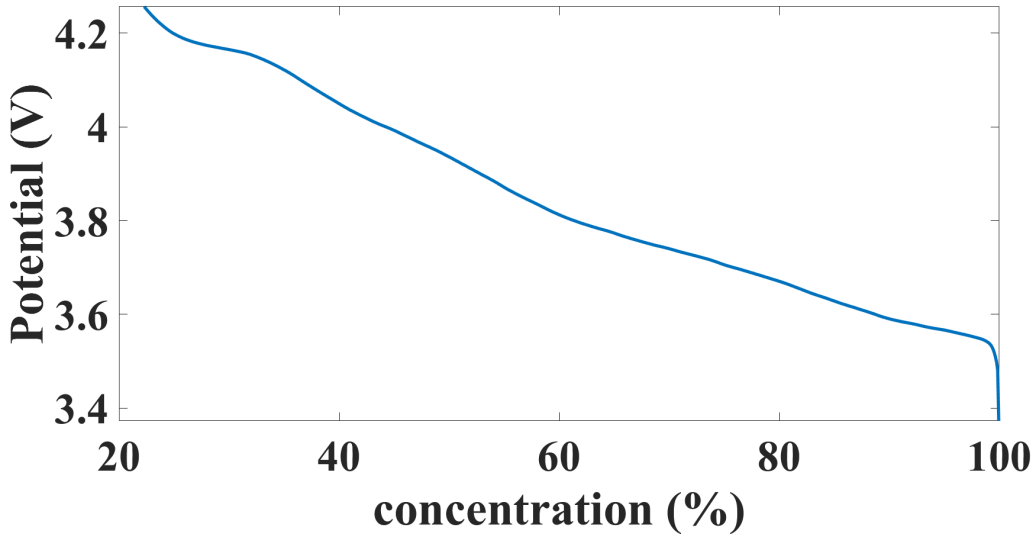

Figure 2.6: The potential versus concentration (%) of Lithium of NMC-811.

2.3.3 LFP

$LiFePO_4(LFP)$ has almost the same theoretical capacity as the NMC-111 at 165 mAh/g, however the potential levels of the chemistry is lower than both the NMC-111 and NMC-811 and as such contains a lower energy and power density than them. However, the benefits of the LFP are that the economical and environmental cost of producing a cell is significantly lower than the NMC cathodes[42] [41]. The LFP cathode also lacks the Cobalt material and thus does not contribute to the negative aspects of the Cobalt extraction process. The characteristic behaviour of the LFP differs from both NMC cathodes as they utilize 3-dimensional diffusion pathways while LFP only utilizes a 1D pathway for diffusion [13].

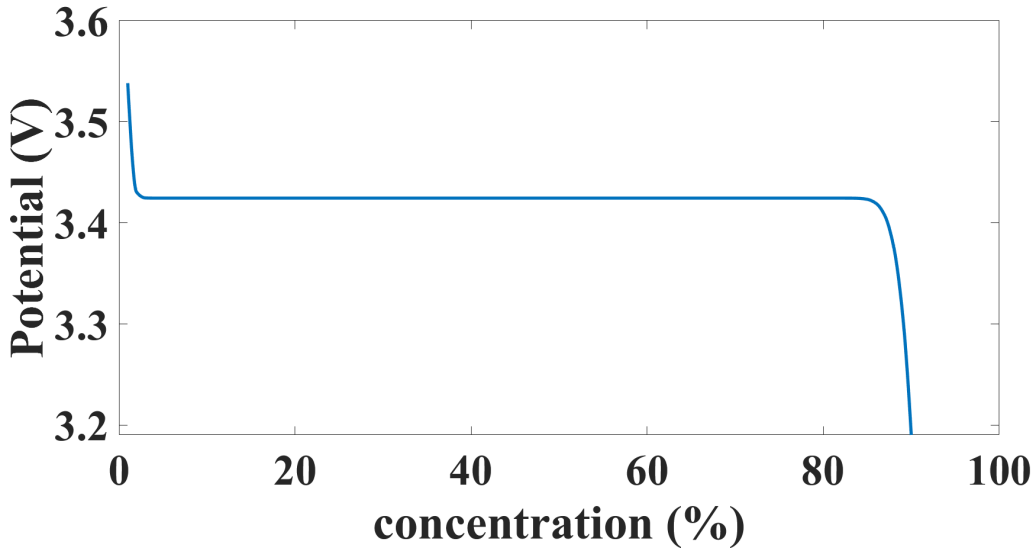

Figure 2.7: The potential versus concentration (%) of Lithium of LFP.

2.3.4 Capacity ratio

To prevent the growth of the SEI layer, the capacity of the negative electrode has to be higher than the positive so that all lithium ions can be properly intergrated into the negative electrode during charge. In order to minimize the amount of material required for each cell, efforts has been made to decrease the ratio between positive electrode capacity and negative electrode capacity, also known as the N/P-ratio. The lowest ratio in batteries of today is an N/P-ratio $1:1.1$, meaning that there is 10% more capacity in the negative electrode than the positive. SEI growth is still experienced at this N/P-raio for high currents and thus, a discussion of increasing the N/P-ratio to $1:1.2$ is valid. For this thesis, however, aging is not investigated and thus an N/P-ratio of $1:1.1$ is chosen[14][17]. Using the N/P ratio, the length of the anode can be calculated as follows

$$L_{An} = \frac{1.1 L_{cath} A_{jelly} \rho_{cath} \varepsilon_{cath} Q_{cath}}{A_{jelly} \rho_{an} \varepsilon_{an} Q_{an}} \tag{2.28}$$

where, 1.1 is the N/P ratio, A_{jelly} is the area of the jelly roll, $\rho_{cath}(kg/m^3)$ and $\rho_{an}(kg/m^3)$ are the density of the cathode and anode respectively. ε_{cath} and ε_{an} are the volume fraction of the cathode and anode, while Q_{cath} and Q_{an} are the usable capacity. Finally L_{cath} and L_{an} are the length of the cathode and anode respectively. The inherent capacity of the cell is determined by the capacity of the cathode as it has a lower ratio compared to the anode.

2.4 Electric circuit model

The internal behaviour of a lithium ion battery can be modelled as an open circuit with a DC voltage source in series with a resistance and several RC parrallel circuits as can be seen in figure 2.8. In the first circuit of figure 2.8 R_0 represents the internal resistance, C_{th} represents the transient response during charge and discharge of the battery and R_{th} represents the polarisation resistance of the battery [37]. The second circuit is a more complex circuit where R_0 still represents the internal resistance, R_{pa} represents electrochemical polarisation resistance, R_{pc} represents concentration polarisation resistance, C_{pa} represents the transient response during charge/discharge and C_{pc} represents the polarisation characteristics[37].

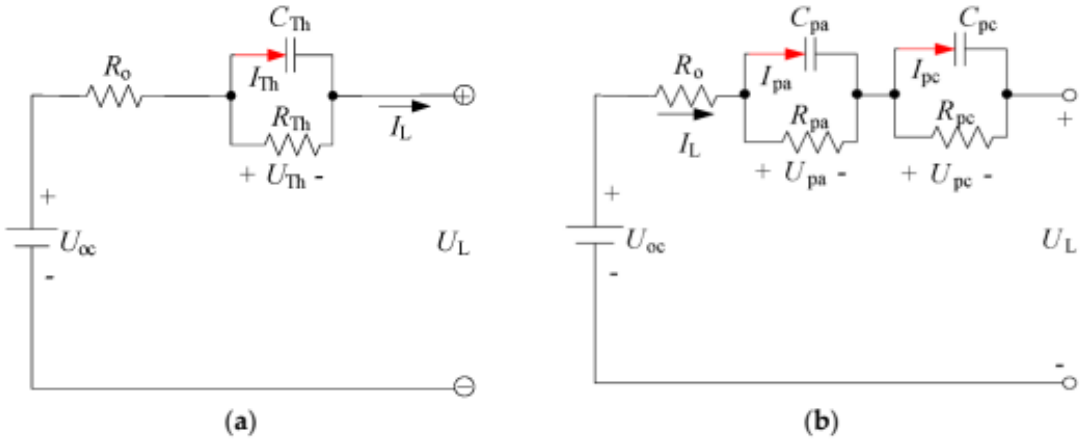

Figure 2.8: Two equivalent circuit models of a battery, figure taken from article by M.-K. Trahn et. al.[37]

Studies has shown that the optimal ECM circuit in simulation aspects for EVs was the first order circuit displayed in 2.8 with only one RC ciruit for the chemistries as stated in [37]. The parameters of the ECM can be acquired by performing a "Galvanic Intermittent Titration Technique" test (GITT test) on the battery. A GITT test is performed by applying a current pulse to a battery followed by a relaxation period where no current is applied which allows the performer of the test to see the charge/discharge characteristics of the battery. This test is performed at SOC levels ranging from 100% to 0% as the parameters of the equivalent circuit are SOC-dependent. Figure 2.9 and 2.10 shows a GITT test being performed for an NMC-811/Graphite cell and by analysing each spike of the discharge curve in Figure 2.10, the battery parameters for the respective SOC level can be acquired.

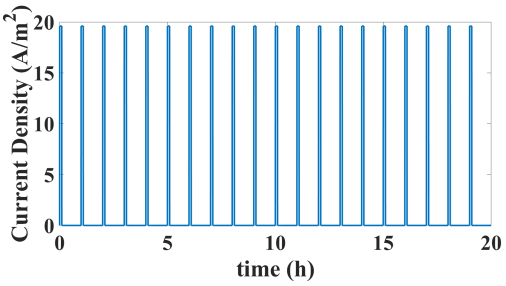

Figure 2.9: Current density pulse setup for a GITT test with 20 discharge spikes.

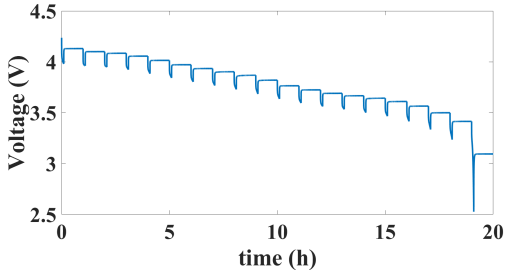

Figure 2.10: Voltage behaviour during GITT test with 20 discharge spikes.

The equations necessary to acquire the equivalent circuit parameters are presented in equation 2.29 through 2.31. V_j represents the voltage output from the battery, $U_{i,j}$ represents the voltage over i number of RC-links respectively and I_j is the applied voltage pulse. In figure 2.11 E_1 and E_2 are presented, E_1 represents the voltage drop over the internal resistance and is equal to $R_0 * I_j$, E_2 represents the voltage over the RC links which for this study is equal to $U_{1,j}$ from equation 2.30. The time constant for an RC-circuit is defined as the time it takes to reach 0.63% of the maximum value and as such the time constant is the time required to go from $E_{1,max}$ to $0.63E_{2,max}$[28].

$$\tau_1 = R_1 C_1 \tag{2.29}$$

$$V_j = OCV - R_0 I_j - U_{1,j} \tag{2.30}$$

$$U_{1,j+1} = exp(-\frac{\Delta t}{\tau_1})U_{1,j} + R_1(1 - exp(-\frac{\Delta t}{\tau_1}))I_j \tag{2.31}$$

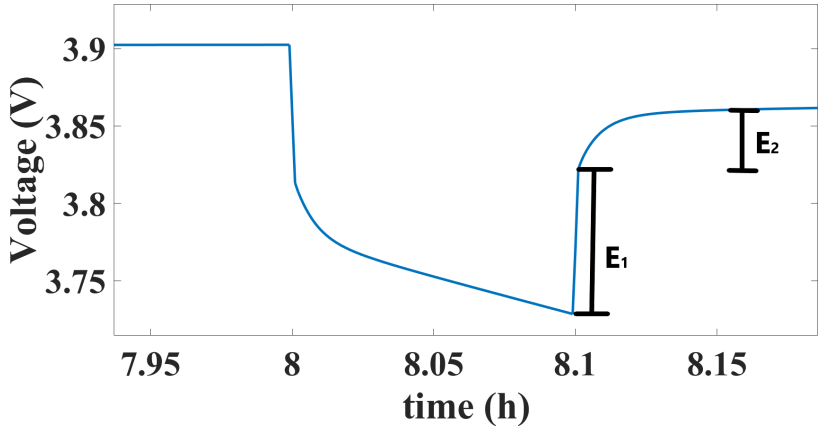

Figure 2.11: Pulse discharge where E_1 represents the voltage over the internal resistance R_0 and E_2 represents the voltage over the RC-links.

2.5 Vehicle dynamics

As the performance of the lithium ion battery is based on a vehicle model, sufficient knowledge regarding vehicle dynamics is required and will be presented in this section. The simulation model used in this thesis is a Quasi Stationary Model (QSS), meaning that the input of data will be in the form of a drive cycle, which places demands on the different vehicle dynamics which ultimately places demands on the battery. The equations described in this section will therefore reflect the dynamics based on the QSS model [45].

2.5.1 Drive Cycle

A drive cycle is a collection of data in the form of a time array and a speed array. The time array determines how long time the cycle will be simulated and the speed array simulates the speed of the vehicle at the corresponding time instance. The speed is put through an integration process to acquire the distance traveled and the speed also goes through a derivative process to acquire the acceleration information of the vehicle.

2.5.2 Chassis Dynamics

The chassis dynamics describes the rotational acceleration, torque and speed of the wheel as described in

$$\omega = \frac{v_{car}}{r_{wheel}} \tag{2.32}$$

$$\frac{d\omega}{dt} = \frac{dv_{car}}{dt}\frac{1}{r_{wheel}} \tag{2.33}$$

$$T = F * r_{wheel} \tag{2.34}$$

where, $v_{car}(m/s)$ is the speed acquired from the drive cycle, $r_{wheel}(m)$ is the radius of the wheel. $\omega(rad/s)$ is the rotational speed of the wheel, $T(Nm)$ is the torque placed on the vehicle and $F(N)$ represents the external forces exercised by the vehicle. The external forces are presented in the form of rolling resistance, aerodynamics resistance and inertia [18].

2.5.2.1 Rolling resistance

The force that the vehicle experiences due to the friction of the road is modelled with a constant friction coefficient for the entire driving cycle and the impact of this force is controlled by a switch that turns on when the speed acquired from the drive cycle has a value higher than zero. The expression for the rolling resistance is displayed in

$$F_{roll} = mgC_r cos(\alpha) \tag{2.35}$$

where, $F_{roll}(N)$ is the rolling resistance, $m(kg)$ is the mass of the vehicle, $g(m/s^2)$ is the acceleration of gravity, C_r is the rolling friction coefficient and $\alpha(rad)$. The drive cycle does not take any consideration to the difference of force experienced during incline or decline of the road, hence α will be zero and thus $\cos(\alpha)$ will be equal to one for this thesis [18].

2.5.2.2 Aerodynamic resistance

A simplified equation to simulate the aerodynamics of the vehicle is used in this thesis since precise modelling of air flow is very complex especially when considering the different shape of different vehicles. The simplified equation is presented as

$$F_a = \frac{1}{2}\rho_a C_d A_f (v_{car} - v_{wind})^2 \tag{2.36}$$

where $F_a(N)$ represents the aerodynamic drag force, $\rho_a(kg/m^3)$ represents the air density, C_d is the aerodynamic drag coefficient, $A_f(m^2)$ is the cross-sectional area of the car, $v_{car}(m/s)$ is the speed of the car and $v_w ind(m/s)$ is the speed of the wind in the direction traveled by the vehicle. The air density chosen for this thesis is $1.225(kg/m^3)$ which represents standard air density at $15°C$ and standard atmospheric pressure of $1013.25Pa$ [18].

2.5.2.3 Inertia

The force accelerating the vehicle and the force of the inertia are represented as

$$F_{acc} = ma \tag{2.37}$$

$$F_{iner} = ma\frac{m_r ot}{100} \tag{2.38}$$

Where $F_{acc}(N)$ is the accelerating force, F_{iner} is the force from the inertia. $m(kg)$ is the mass of the vehicle, $a(m/s^2)$ is the acceleration of the vehicle and $m_{rot}(\%)$ is the rotating mass of the vehicle [45].

2.5.3 Transmission Dynamics

The purpose of a transmission system in the vehicle is to be able to scale the magnitude of the torque affecting the wheels down to a level that can be handled by the electrical machine. For this thesis a fixed gear ratio is used to model the transmission of the vehicle. The expression for the speed and acceleration exchange are presented as

$$\omega_{trans} = g_r \omega_{wheel} \tag{2.39}$$

$$\frac{d\omega_{trans}}{dt} = g_r \frac{d\omega_{wheel}}{dt} \tag{2.40}$$

where $\omega_{trans}(rad/s)$ is the rotational speed of the electrical machine, $\omega_{wheel}(rad/s)$ is the rotational speed of the wheel and g_r is the gear ratio of the transmission. The

torque is calculated in two instances, once when energy is flowing from the engine to the wheel and once when the energy is flowing from the wheel to the engine. The equations used to calculate the torque when energy is flowing from the engine to the wheel and when it is flowing from the wheel to the engine are described in

$$T_{trans+} = \frac{1}{g_r \eta_g}(\frac{P_{idle}}{\omega_{wheel}} + T_{wheel}) \tag{2.41}$$

and

$$T_{trans-} = \frac{\eta_g}{g_r}(\frac{P_{idle}}{\omega_{wheel}}\eta_g + T_{wheel}) \tag{2.42}$$

respectively. Here, $T_{trans+}(Nm)$ is the torque when energy is flowing from the engine to the wheel, $T_{trans-}(Nm)$ is the torque when energy is flowing from the wheel to the to the engine. g_r is the gear ratio, η_g is the efficiency of the transmission, $P_{idle}(W)$ is standing for the losses in the transmission due to idling, $\omega_{wheel}(rad/s)$ and $T_{wheel}(Nm)$ are the speed and torque values received from the dynamics of the chassis [45].

2.5.4 Electric Machine Dynamics

The electric machine is the driving force of the EV and can have varied designs, with the induction machine or permanent magnet synchronous machine (PMSM) being two of the more common ones. The modelling of the electric machine is complex and varied depending on which electric machine is chosen and since the choice of electric machine is not of interest for this thesis, a general efficiency map is used. This efficiency map uses the torque and the speed from the transmission block and gives an efficiency output which is then multiplied with the speed and torque of the electric machine to give the power required by the battery as showcased in

$$P_{EM} = T_{EM} * \omega_{EM} * \frac{1}{\eta_{EM}(T_{EM}, \omega_{EM})} \tag{2.43}$$

with the total torque of the electrical machine, T_{EM}, being derived from

$$T_{EM} = T_{trans} + \frac{d\omega_{EM}}{dt} * J_{eng} \tag{2.44}$$

Here, $T_{trans}(Nm)$ is the torque acquired from the transmission system, $J_{eng}(kg/m^2)$ is the inertia of the engine and $\omega_{EM}(rad/s)$ is the speed of the engine. $P_{EM}(W)$ is the power requirement of the battery.

The efficiency map is usually only displayed for the case of positive torque and speed, however, the map can be applied for cases of negative speed or torques as well according to

$$\eta_{EM}(T_{EM}, \omega_{EM}) = \eta_{map} \quad for \quad \{T_{EM} > 0; \quad \omega_{EM} > 0\} \tag{2.45}$$

$$\eta_{EM}(T_{EM}, \omega_{EM}) = -\eta_{map} \quad for \quad \{T_{EM} > 0; \quad \omega_{EM} < 0\} \tag{2.46}$$

$$\eta_{EM}(T_{EM}, \omega_{EM}) = \frac{1}{\eta_{map}} \quad for \quad \{T_{EM} < 0; \quad \omega_{EM} > 0\} \tag{2.47}$$

$$\eta_{EM}(T_{EM}, \omega_{EM}) = -\frac{1}{\eta_{map}} \quad for \quad \{T_{EM} < 0; \quad \omega_{EM} < 0\} \tag{2.48}$$

where, η_{map} is the efficiency as showcased when speed and torque is positive and η_{EM} is the efficiency of the vehicle for the presented case [45].

3
Case Setup

In this section, the process of creating the required models and the tests required to facilitate a result will be presented as well as assumptions and simplifications made during the thesis.

3.1 COMSOL model

The battery creation process occurs in the Software "COMSOL Multiphysics 5.6" which uses physical relations in the form of mathematical equations to simulate the behaviour of the subject of the study. To simulate the cell behaviour of the three different battery chemistries, a 1D model is utilized and with the use of the equations for voltage calculation, mass transport and current flow, provided by the battery node in the COMSOL software, the behaviour of a cell when a reference current density is applied to the model is described. To simulate discharge or charge of the cell, the anode is connected to a ground and the cathode is connected to a current density source which represents the current flowing in the external circuit of the battery where the direction of the current density decides if there is a discharge or charge occurring. Firstly, a prototype cell is created to facilitate that the simulations operates properly, this cell was created based on a cell used in [30] in order to produce a reality based simulation model. The model is comprised of a NMC-811 cathode and a Graphite anode, where the parameters are displayed in table 3.1.

Table 3.1: Battery design parameters of the first battery cell

	Cathode	Separator	Anode
Thickness L	66.2 μm	12 μm	86.7 μm
Particle radius r_p	3.8 μm		6.1 μm
Active material fraction ϵ_s	74.5 %		69.4 %
Inactive fraction $\epsilon_{s,na}$	8.4 %		9 %
Porosity ϵ_l	17.1 %	40%	21.6 %
Film resistance R_{film}	0.0%		0.0035 %

3.2 Curve fitting

Once the prototype cell was created, the parameter acquisition process was started by performing a GITT test on the cell. The setup for the GITT test was a current pulse with 1C magnitude over a time of 5% of an hour repeated 20 times to get a

full discharge of 100 % SOC to 0% SOC. The data acquired from the GITT test was exported to MATLAB through the "Livelink for MATLAB" function in COMSOL. This data was then processed in MATLAB to acquire the voltage-time characteristics that occur when the current pulse is released during charge and discharge for the different SOC levels. With the use of equation 2.29 through 2.31 preliminary values for the parameters R_0, R_1, and C_1 were calculated by analysing the plot data and choosing values based on equations 2.29 through 2.31. However, the preliminary values acquired through this method are not accurate enough as a plot of the simulated model as shown in figure 3.1.

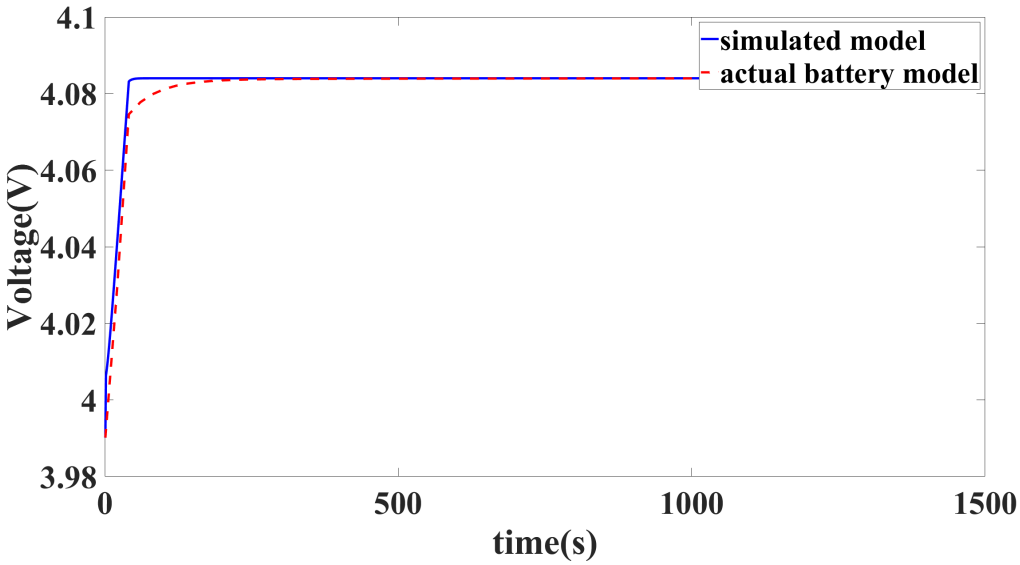

Figure 3.1: Voltage characteristics of the model with the calculated preliminary values of the parameters (blue) versus the actual battery model (red).

A better approximation of the battery parameters is needed to properly model the battery. This approximation will occur in the form of a curve fitting algorithm using the "nlinfit" function in MATLAB. The algorithm used for this curve fitting is a modified version of the algorithm provided in [37]. The algorithm uses the preliminary parameters calculated earlier as input values and through the use of nonlinear regression fits the parameters to the curve. As can be seen in figure 3.2, the algorithm has improved the parameter estimation greatly with the average error of the algorithm being between $2 - 0.5\%$.

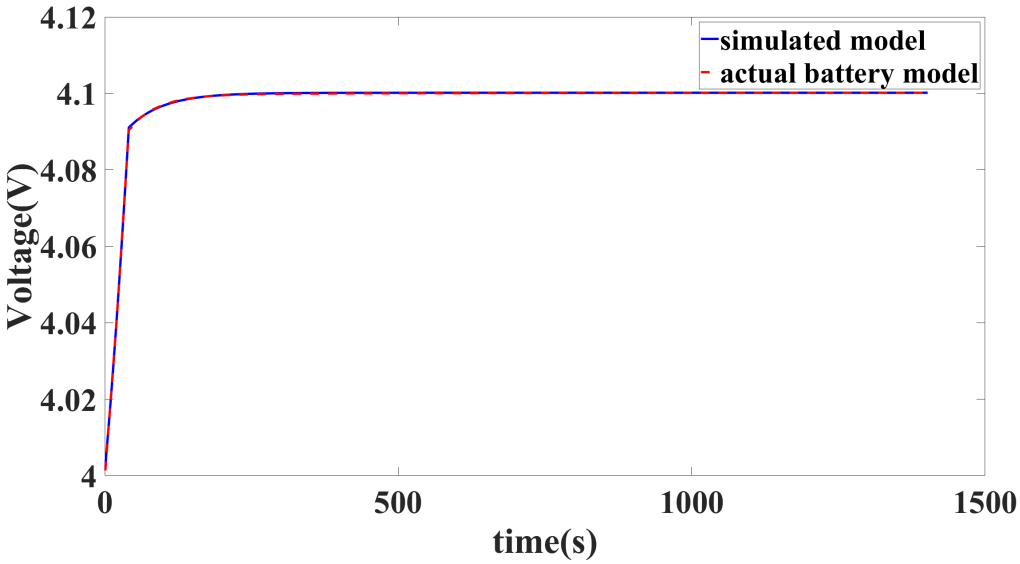

Figure 3.2: Voltage characteristics of the model with the parameters acquired through the nonlinear regression model (blue) versus the actual battery model (red).

The resistance and capacitance values gained from this algorithm are acquired by using the 1C current density and multiplying it with the surface area of the jelly roll.

3.3 Battery cell modelling

When the GITT test and the nonlinear regression algorithm worked as intended on the prototype cell, the different batteries that are to be tested has to be created. As previously stated three different battery chemistries are subject to test for the thesis, these being NMC-811, NMC-111 and LFP. The thesis focus is to compare the battery performance for battery cells with differing thicknesses and as such five batteries with varying thicknesses are created for each cell chemistry. The prototype electrode was chosen as a reference when creating the different cells thus two cells with lower cathode thicknesses and two cells with higher cathode thicknesses were created. The thicknesses chosen for the cells are displayed in table 3.2 and henceforth to be referred to with the thickness of the cathode. These thicknesses will be the same for all chemistries.

Table 3.2: Cathode thickness for the different batteries for the varying chemistries

	Cathode thickness [μm]
Battery 1	35
Battery 2	50
Battery 3	66.2
Battery 4	80
Battery 5	95

The N/P ratio of this thesis is 1 : 1.1 which will be used when modelling the thickness of the anode. The anode thickness will thus be displayed in table 3.3.

Table 3.3: Anode thickness for the different batteries for the varying chemistries

Cathode thickness [μm]	Anode thickness [μm]
$NMC-811$ 35	37.25
$NMC-811$ 50	53.2
$NMC-811$ 66.2	70.45
$NMC-811$ 80	85.1
$NMC-811$ 95	101.1
$NMC-111$ 35	29.29
$NMC-111$ 50	41.85
$NMC-111$ 66.2	55.4
$NMC-111$ 80	66.96
$NMC-111$ 95	79.5
LFP 35	28.7
LFP 50	40.99
LFP 66.2	54.27
LFP 80	65.88
LFP 95	77.88

When designing the cells for the different chemistries, the aspects considered when selecting the parameters were to maintain the active and inactive fraction, the porosity and the N/P ratio across all cells to ensure that the cells can be compared properly based on the parameters from the prototype cell. The particle size will be chosen to be similar for all chemistries if the literature shows that these values are appropriate. The active particle radius for the NMC-111 is chosen to be the same as for the NMC-811 which article [26] supports, however, the particle radius for the LFP has to be changed as several studies show that the average particle size has a radius range between $300 - 500nm$[21][26], and a particle radius of $380nm$ was chosen as it is exactly an order of magnitude lower than the particle radius of NMC-111 and NMC-811. The upper cut-off voltage for the cells can be showcased in table 3.4, where, the voltage levels were chosen in order to ensure the maximum capacity for each chemistry without compromising the stability of the structure.

Table 3.4: Initial voltage levels for the different chemistries.

	NMC-811	NMC-111	LFP
Voltage	4.2	4.2	3.4

The 100 % to 0 % discharge occurs from the voltage level set in table 3.4 until it reaches the lower cut-off voltage which is decided to be $2.5V$ in order to avoid SEI build up. When the entire voltage range is covered during the GITT test for all cells, the data acquired through the GITT test is treated through the nonlinear algorithm in MATLAB to acquire the parameters for the entire SOC range.

3.3.1 Jelly roll dimensions

Applying the theory of Archimedes spiral to the overall thickness of the cell, the length of the jelly roll can be acquired. The length of the jelly roll for each individual cell is displayed in table 3.5. The height of the jelly roll does not vary for the different batteries and will, thus, have a height of $5.8cm$.

Table 3.5: Jelly roll length for the different batteries for the varying chemistries.

	Jelly Roll length [cm]
$NMC-811 \quad 35\mu m$	99.82
$NMC-811 \quad 50\mu m$	75.9
$NMC-811 \quad 66.2\mu m$	60.34
$NMC-811 \quad 80\mu m$	51.37
$NMC-811 \quad 95\mu m$	44.20
$NMC-111 \quad 35\mu m$	108.6
$NMC-111 \quad 50\mu m$	83.25
$NMC-111 \quad 66.2\mu m$	66.49
$NMC-111 \quad 80\mu m$	56.75
$NMC-111 \quad 95\mu m$	48.96
LFP $35\ \mu m$	109.32
LFP $50\ \mu m$	83.86
LFP $66.2\ \mu m$	66.99
LFP $80\ \mu m$	57.1
LFP $95\ \mu m$	49.36

3.4 Energy and Power Density

In order to acquire the power and energy density of the cells, numerous discharges from 100% to 0% SOC were performed, each with a different C-rate in a range from 0.01C to 10C. The current density that represent 1C for the different cells are acquired by performing a full discharge that lasts an hour where the result is displayed in table 3.6. The simulation multiplies the current density for each iteration with the voltage of the cell and the area of the jelly roll to obtain the power per cell. In order to access the power density of the cell, the power is divided

by the weight of the cell. The energy density of the cell is acquired by performing an integration for each iteration of the power density based on the time it takes to complete an iteration. To visualise the trade-off between the energy density and power density, a curve is produced by interpolating all simulation instances called the ragone plot.

Table 3.6: 1C for the different cells.

1C current density [A/m^2]	NMC-811	NMC-111	LFP
35μm	20.37	16.01	12.95
50μm	29	22.95	18.49
66.2μm	38.37	30.4	24.5
80μm	44.5	36.8	28.8
95μm	43.5	43.1	28.8

Through this test the capacity of the individual cells is acquired by multiplying the current with the time it takes to complete a simulation iteration. The capacity of the cell will rapidly decrease once the characteristic diffusion length is shorter than the electrode length and therefore the capacity of the cell will be defined as the capacity of the cell at the iteration before this decrease. An example of this can be displayed in figure 3.3, where the capacity selection is simulation instance before the steep decline.

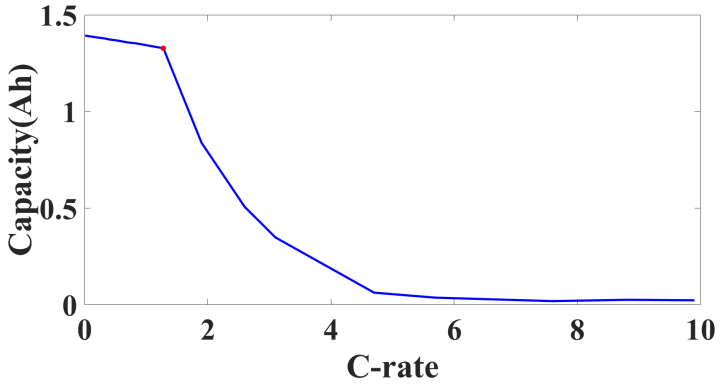

Figure 3.3: Capacity behaviour of Lithium ion cell.

This explains why the 1C current density stop increasing at a certain thickness as the capacity decline occurs at a current density lower than the 1C current density.

3.5 Vehicle Model

The testing and comparison between the different batteries are performed using a SIMULINK model of an electric vehicle. The model is built using the quasi-stationary toolbox published by ETH Zürich which uses a drive cycle as input to the vehicle model. The vehicle is compromised of four different simulation blocks each representing a key characteristic of the vehicle. The first block is the vehicle block which uses the speed and acceleration data acquired from the drive cycle to calculate the torque, the rotational speed and the rotational acceleration of the wheel. The second block is a simple transmission block which applies a fixed gear ratio to the input from the vehicle block to ensure a proper input to the electric machine block. The electric machine block uses the outputs from the transmission block in combination with a look-up table for efficiency to calculate the power required from the battery. The last block is the battery block, which uses the power requirement as an input and calculates the energy consumption as an output. It is in this battery block the ECM of the battery cells will be simulated and where the cells will be combined into a battery pack.

The validity of the vehicle data is important for the test to be as close to reality as possible, the parameters for the vehicle excluding the battery are therefore incorporated from an actual vehicle. The vehicle chosen for parameter acquisition is a "Nissan Leaf 15" [19].

3.5.1 Drive Cycle

The drive cycle used in this thesis will be the "Worldwide harmonized Light vehicles Test Procedure" (WLTP) drive cycle produced by UNECE, which is a common drive cycle used in vehicle testing today, which replaced the old drive cycle "New European Drive Cycle" (NEDC) 2017 [43].

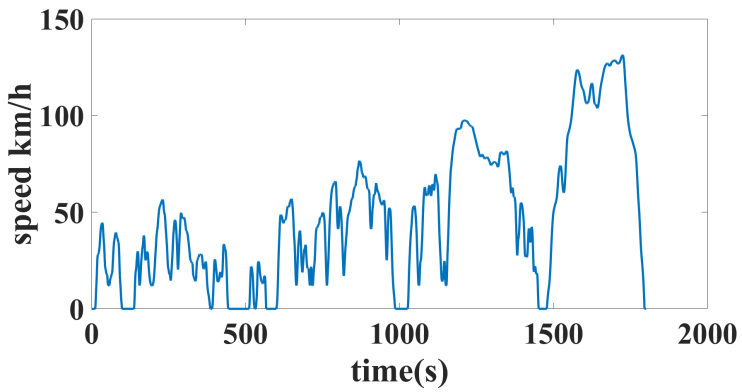

Figure 3.4: WLTP Drive Cycle.

3.5.2 Vehicle Block

The input data acquired from the driving cycle is processed in the vehicle block to produce the rotational speed, acceleration and torque of the wheel. The SIMULINK model utilizes the equations 2.35 through 2.38 as presented for the chassis dynamics in the theory section in order to calculate the torque and speed of the wheel of the vehicle. The Model is displayed in 3.5.

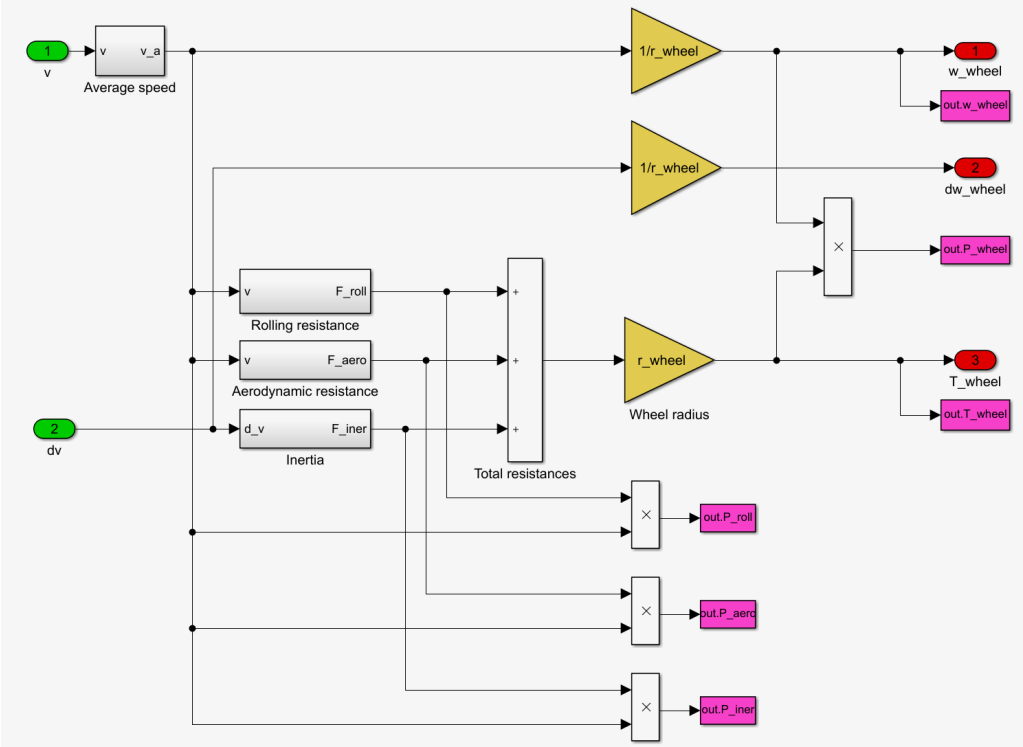

Figure 3.5: Overview of the chassis dynamics impact on the electric vehicle model

3.5.2.1 Mask Data

In the QSS toolbox, the parameters necessary for the simulation can be put into a user-interface called a mask. The input parameters change depending on which block that is being used, the parameters and their respective values are presented in table 3.8. The typical value of the rolling friction coefficient and the drag coefficient have a standardized value between 0.006-0.014 and 0.25-0.35 respectively, and for simplicity's sake, the value at the midpoint was chosen for both [23][18]. To acquire proper performance when each battery is applied, a simulation will be performed where the weight of the original battery of the Nissan Leaf is applied. This is to find initial values of power consumption for the battery, for which the battery pack can be modelled after. The weight will then be replaced with the equivalent weight of each battery pack in further simulations. The weight displayed here is the weight

of the original Nissan Leaf, where the 273 kg is the weight of the original battery.

Table 3.7: Mask data of the vehicle block.

Total mass of the vehicle [kg]	1144 + 273
Rotating mass [%]	5
Vehicle cross section [m^2]	2.27
wheel diameter [m]	0.6319
Drag Coefficient [-]	0.3
Rolling friction Coefficient [-]	0.010

3.5.3 Transmission Block

In this simulation the transmission is handled by the simple transmission block of the QSS toolbox which uses a fixed gear ratio to increase the speed and acceleration data and to decrease the torque. The SIMULINK model utilizes (2.39) through (2.42) with the switching between (2.41) and (2.42) being done by a switch that uses T_{wheel} as input, when T_{wheel} is zero and above (2.41) is used and when below, (2.42) is used. To avoid idling losses when the vehicle is in standstill, a switch for the ω_{wheel} input is intregated into the model where a minimum wheel speed is set as input to the switch. If the speed acquired from the vehicle block is lower than the minimum wheel speed, the speed input to (2.41) and (2.42) is infinite, making the idling losses be zero. The SIMULINK model is presented in figures 3.6 and 3.7.

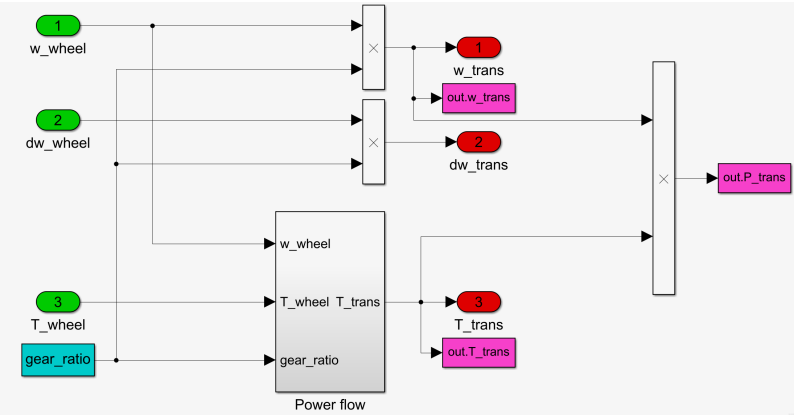

Figure 3.6: Overview of transmission model.

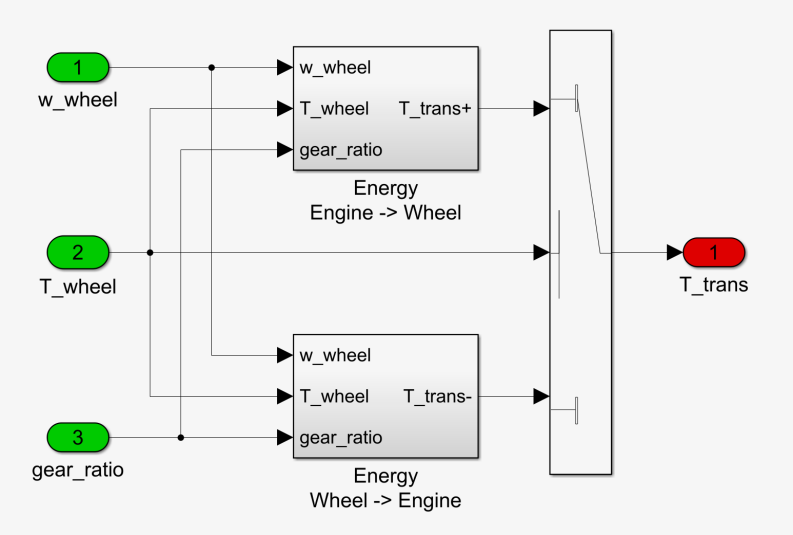

Figure 3.7: Switching mechanism of the torque calculation.

3.5.3.1 Mask data

The value of the gear ratio is acquired from the "Nissan Leaf 15" [19], the value of the efficiency is assumed to be 95% according to [4] [18].

Table 3.8: Mask data of the simple transmission block.

Gear ratio [-]	8.1398
Efficiency [-]	5
Idling losses (friction) [W]	20
Minimum wheel speed beyond which losses are generated [rad/s]	1

3.5.4 Electric motor block

The QSS toolbox utilizes a look-up table in order to portray the efficiency map of the electric machine, which is showcased in 3.8.

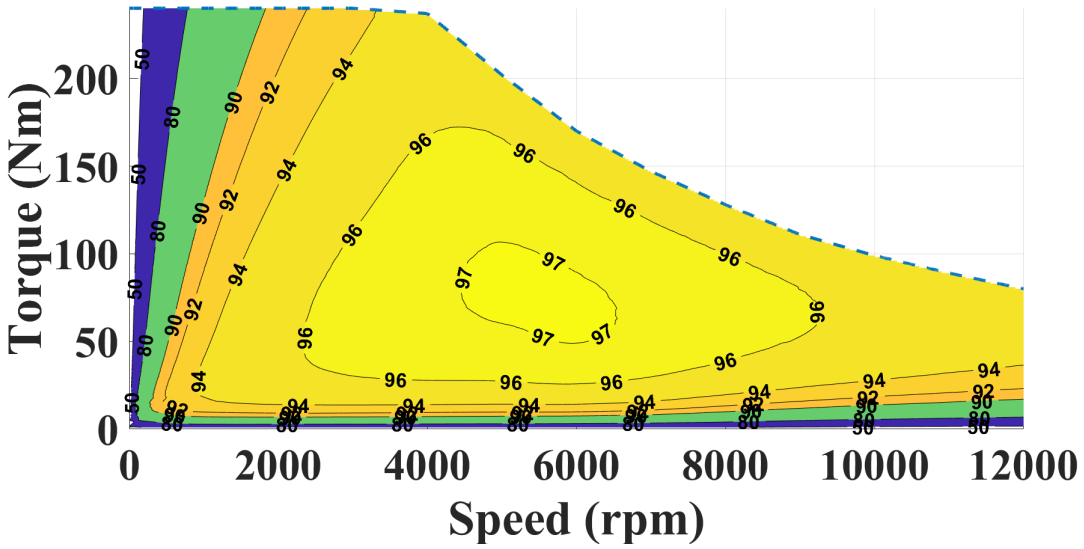

Figure 3.8: Efficiency map of Electric machine used in this thesis.

The equations used to apply the efficiency map to acquire the power demand from the battery are displayed in order to acquire the power demand of the battery with the application of the efficiency map, equations 2.43 through 2.48 are applied to the model. The inertia for the Nissan Leaf 2015 engine could not be found, so a value of $J_{eng} = 1.53kg/m^2$ was chosen, based on a study where a vehicle with similar capabilities to a Nissan Leaf Model was investigated [20].

While, the upper limits of the electric machine used in Nissan Leaf 2015 has been identified, sufficient information regarding the efficiency mapping could not be found for this particular EV [19]. The efficiency mapping provided in the QSS toolbox was not sufficient as the electric machine reached speeds outside of the defined range of the efficiency mapping. An efficiency map was thus provided by the institution of Power Electric Engineering at Chalmers, that fulfilled the demands of the vehicle, while not exceeding the dimensions of the electric machine used in Nissan Leaf 2015. The SIMULINK model of the electric machine can be viewed in figure 3.9.

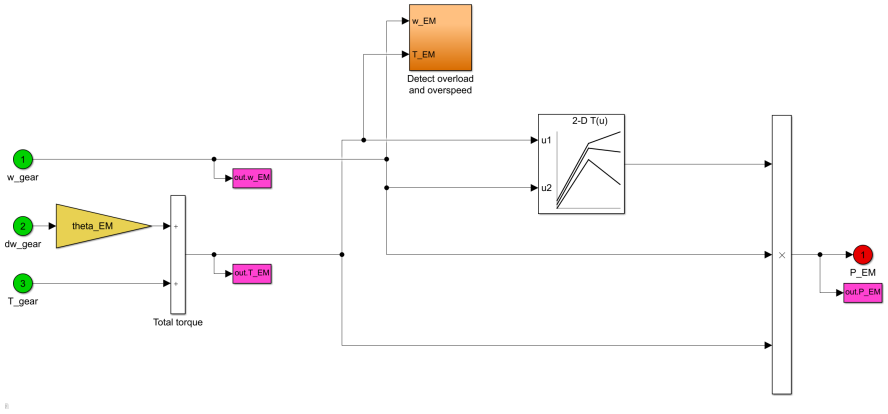

Figure 3.9: Electric machine block of the simulink model.

3.5.5 Battery

With the focus off this thesis being the implementation of the battery into an EV, most focus of the SIMULINK model has been placed on the battery implementation. The implementation of the parameters acquired through the GITT test is done by lookup-tables, where the model uses the state of charge of the battery as an input and gives the values of the parameters as output based on the state of charge. The battery will be modelled with the terminal voltage of the ECM as the output. The power input from the electric machine block will be divided with the voltage output to acquire the current going through the battery and will be used as an input to the battery model [11]. An overview of the battery simulation model is provided in figure A.1 in the appendix.

3.5.5.1 State of charge calculation

The SOC will be calculated according to

$$SOC = SOC_0 + \int \frac{100I}{3600Q} dt \tag{3.1}$$

where, $SOC(\%)$ is the state of charge of the battery, SOC_0 $(\%)$ is the level of SOC at the start of discharge which will be 100 $(\%)$ for this thesis as discharge of the entire SOC range is of interest for the goal of it. I (A) is the current going through the battery and Q (Ah) is the capacity of the battery and represents the C-rate of the battery, which is then multiplied by 3600 to convert the unit from Ah to As, finally the value 100 is to convert the integral to a percentage value. The value of the capacity is acquired through a lookup-table which uses the data acquired through the ragone plot to map the the capacity as a function of the input current according to

$$Q_k = \frac{I_k t_k}{3600} \tag{3.2}$$

where, $Q_k(Ah)$ is the capacity of the battery at iteration k of the ragone plot. $I_k(A)$ is the current at iteration k and $t_k(s)$ is the time required for the battery to be fully discharged at iteration k.

3.5.5.2 ECM implementation

From the GITT test, the values for V_{OCV}, R_0, R_1 and C_1 has been acquired for the entire SOC range and, thus, the lookup-tables for these four parameters uses the SOC level as input to acquire the values of the parameters for the corresponding SOC. The terminal voltage is calculated according to

$$V_{term} = V_{OCV} + V_0 + V_1 \tag{3.3}$$

where, $V_{term}(V)$ is the terminal voltage, $V_{OCV}(V)$ is the open circuit voltage, $V_0(V)$ is the voltage drop over the resistance R_0 and $V_1(V)$ are the voltage drop over the RC link of R_1 and C_1. The calculations for voltage V_0 and V_1 are shown

$$V_0 = R_0 I \tag{3.4}$$

and

$$V_1 = \frac{1}{s}\left[\frac{I}{C_1} - \frac{V_1}{R_1 C_1}\right] \tag{3.5}$$

respectively.

3.5.5.3 Loss Calculations

To calculate the losses of the battery, the loss of each individual component will be analysed. The losses are found as

$$P_{loss} = P_{R_0} + P_{R_1} \tag{3.6}$$

$$P_{R_0} = R_0 * I^2 \tag{3.7}$$

$$P_{R_1} = R_1 * I_1^2 \tag{3.8}$$

where,

$$I = I_1 + I_2 \tag{3.9}$$

$$I = \frac{V_0}{R_0} \tag{3.10}$$

$$I_1 = \frac{V_1}{R_1} \tag{3.11}$$

$$I_2 = \frac{V_0}{R_0} - \frac{V_1}{R_1} \tag{3.12}$$

The total losses of the battery are then divided by the output power of the OCV voltage source to gain the efficiency of the battery, according to

$$P_{OCV} = V_{OCV} I \tag{3.13}$$

and

$$\eta_{Batt} = \frac{P_{loss}}{P_{OCV}} \tag{3.14}$$

3.5.5.4 Battery Pack dimensioning

The battery pack is comprised of multiple battery cells which can either be connected in series or in parallel. The dimensions of the battery pack is decided based on two factors, the maximum power output of a drive cycle and the energy required to drive the electric vehicle 16 "Worldwide Harmonized Light Vehicle Test Procedure" (WLTP) drive cycles which equate to $372.2km$. The initial dimensioning will be based on the power and energy requirements of the first simulation where the original battery weight is included in the total vehicle weight. The battery weight will then be replaced with the weight of the battery test and if the power or energy of the new battery is not enough to sustain the demand of the test, a new dimensioning of the battery will have to be made based on the new power and energy requirements. By using the optimal energy density and power density point from the ragone plot in combination with the power and energy requirement of the vehicle, the total weight of the battery can be acquired and by dividing the weight requirement with the weight of each individual cell, the number of cells required are achieved.

The battery pack is modelled by creating an equivalent circuit of the battery pack. The equivalent circuit is modelled with the number of cells in series being denoted by the letter n and the number of cells in parallel being denoted by the letter m. The equivalent series resistances can be calculated by using

$$Z_{series} = \sum_{n=1}^{n} Z = n * Z \tag{3.15}$$

$$\frac{V_0}{I} = R_{0,n} = n * R_0 \tag{3.16}$$

$$\frac{V_1}{I} = \frac{1}{\frac{1}{R_{1,n}} + s * C_{1,n}} = n \frac{1}{\frac{1}{R_1} + s * C_1} \tag{3.17}$$

$$R_{1,n} = n * R_1 \tag{3.18}$$

$$C_{1,n} = \frac{1}{n} * C_1 \tag{3.19}$$

Equation (3.19) and (3.18) is a derivation from (3.17). The number of cells in parallel are calculated using

$$Z_{parallel} = \sum_{n=1}^{m} \frac{1}{Z} = m * \frac{1}{Z} \tag{3.20}$$

$$\frac{1}{Z_m} = \frac{1}{R_{0,m} + \frac{1}{\frac{1}{R_{1,m}} + s * C_{1,m}}} = m * \frac{1}{R_0 + \frac{1}{\frac{1}{R_1} + s * C_1}} \tag{3.21}$$

$$R_{0,m} + \frac{1}{\frac{1}{R_{1,m}} + s * C_{1,m}} = \frac{1}{R_0} + \frac{1}{\frac{m}{R_1} + s * C_1 * m} \tag{3.22}$$

$$R_{0,m} = \frac{R_0}{m} \tag{3.23}$$

$$R_{1,m} = \frac{R_1}{m} \tag{3.24}$$

$$C_{1,m} = m * C_1 \tag{3.25}$$

Equation (3.22) is derived from 3.21 and thus the values of $R_{0,n,m}$, $R_{1,n,m}$ and $C_{1,n,m}$ is displayed in

$$R_{0,n,m} = \frac{n}{m} R_0 \tag{3.26}$$

$$R_{1,n,m} = \frac{n}{m} R_1 \tag{3.27}$$

$$C_{1,n,m} = \frac{m}{n} C_1 \tag{3.28}$$

The voltage output of the battery pack will increase for each battery in series and the output current will increase with each battery in parallel and to model this phenomena, the OCV voltage acquired from the lookup-table will be multiplied with the number of cells in series. The input power is then being divided by the output voltage to acquire the current of the equivalent battery pack circuit, which is then sent as input to the battery pack to complete the feedback loop. The SOC calculation section still operates at a cell level and as such the current input to the SOC calculation will be divided by the number of cells in parallel. The selection of the amount of batteries in series is based on the voltage rating of the battery pack, which is 390V according to the data sheet for "Nissan Leaf 2015" provided in [19], where the number of cells in series for each chemistry is displayed table 3.9. The voltage used to calculate this number is the the voltage available at 100% SOC in order to not cause overvoltage issues for the converter, the values can be found in table 3.4.

Table 3.9: Initial voltage levels for the different chemistries.

	NMC-811	NMC-111	LFP
Number of cells in series	93	93	113

3.6 Environmental Impact of Cell Components

The environmental analysis is conducted in a cradle-to-gate method, meaning that only the material extraction and battery production of the cells life cycle will be analysed, which is due to the scope of not analysing the parameter behaviour during the aging of the cell. The environmental analysis is done by comparing the amount materials used in the different batteries to the values provided in the database GREET (2021). The Greenhouse gases, Regulated Emissions, and Energy use in Technologies model (GREET model) is a simulation tool created by Argonne National Laboratory which uses emissions data for the inventory of the LCA analysis to provide the total emissions of the process[41].

The simulation tool is used to simulate LCA under varying conditions, however, the cradle-to gate information that is relevant to this thesis is available in the database that the modelling software is based on and will be showcased in table 3.10. GREET is heavily utilized in the LCA studies for lithium ion battery technology and the data acquired through the GREET database for lithium ion batteries is showcased to be similar to data from other studies according to the LCA litterature study performed by Aichberger et. al.[32]. To analyse the relationship between the losses of the battery and the Greenhouse gas (GHG) emissions, the GHG emissions per kWh is given for two cases in article [36]. One being the Swedishenergy Mix of 40 $gC0_2 - eq/kWh$ and the other one being the South Korean energy mix of 690 $gC0_2 - eq/kWh$ providing a low emission grid and a high emission grid scenario for which the losses will be compared to.

Table 3.10: GHG emission values based on the GREET model.

Material	GHG
NMC-811	16.17 $[kgCO_2 - eq/kg]$
NMC-111	12.88 $[kgCO_2 - eq/kg]$
LFP	4.28 $[kgCO_2 - eq/kg]$
Graphite	4.50 $[kgCO_2 - eq/kg]$
Copper	3.36 $[kgCO_2 - eq/kg]$
Aluminum	7.78 $[kgCO_2 - eq/kg]$
Steel	2.75 $[kgCO_2 - eq/kg]$
Separator	2 $[kgCO_2 - eq/kg]$
Electrolyte	9.6 $[kgCO_2 - eq/kg]$
Assembly	13.3 $[kgCO_2 - eq/kWh]$

3.7 Cost of Cell Components

The cost analysis is performed similarly to the environmental analysis, using a Software called "BatPac Model software" which is a performance and cost analysis tool produced by Argonne National Laboratory [42]. BatPac has been used in several LCA studies for performance analysis as well as cost analysis for lithium ion bat-

teries such as in [35], [38], [29] often in combination with an environmental analysis software such as GREET to complete an LCA analysis and can be considered a reliable source for cost analys. Batpac is an American software and thus the prices are based on the American market. The manufacturing cost is based on the manufacturing process as well as the average salary per hour and the number of cells manufactured in an hour. The BatPac estimation of manufacturing cost is on the lower side on the spectrum as a cost comparison between the American market and the Chinese market assumes a cost per unit to be between 1.88 and 2.19 USD [10].

Table 3.11: Financial cost values based on the BatPac model.

Material	Cost
NMC-811	26 [USD/kg]
NMC-111	25.5 [USD/kg]
LFP	10 [USD/kg]
Graphite	10 [USD/kg]
Copper	1.2 [USD/m^2]
Aluminum	0.2 [USD/m^2]
Case	2.45 [USD/kg]
Separator	0.9 [USD/m^2]
Electrolyte	10 [USD/L]
Manufacturing	1.29 [USD/unit]

4

Analysis

In this section the results acquired through the simulations will be displayed and discussed. Analysis and comparison of the environmental aspects of the different thicknesses and chemistries will also be conducted in this section.

4.1 Battery parameters

Through the use of the nonlinear regression algorithm, parameters for the ECM for all batteries were acquired. These are displayed in figures 4.1 through 4.13. The parameter values of R_0 and R_1 increases with the increase of thickness for all cell chemistries. The NMC-811 and NMC-111 cathodes shows a dramatic increase of resistance and decrease of capacitance below 5% SOC and therefore, the simulation range will occur in the range of 100% to 5% SOC, with the losses below 5% SOC will be analysed individually.

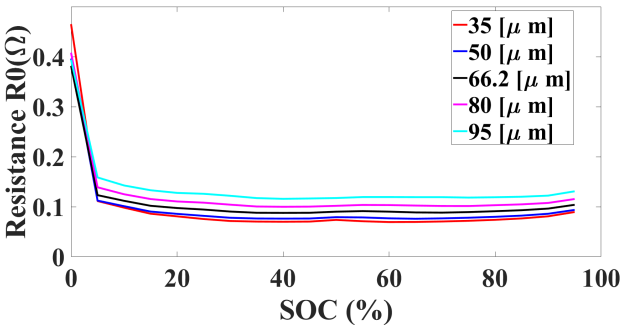

Figure 4.1: Value of R_0 for the entire SOC range for the NMC-811 battery cell.

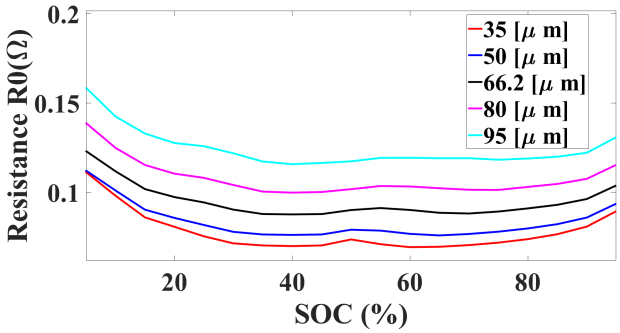

Figure 4.2: Value of R_0 for the SOC range 5 % to 95 % for the NMC-811 battery cell.

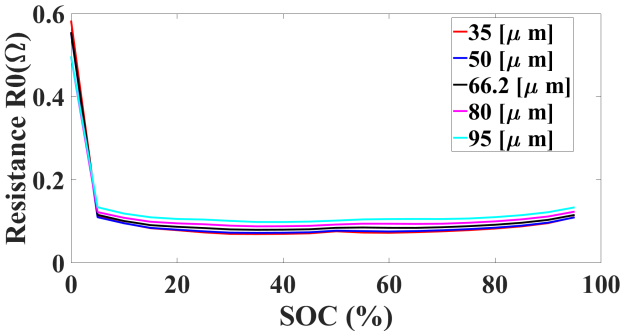

Figure 4.3: Value of R_0 for the entire SOC range for the NMC-111 battery cell.

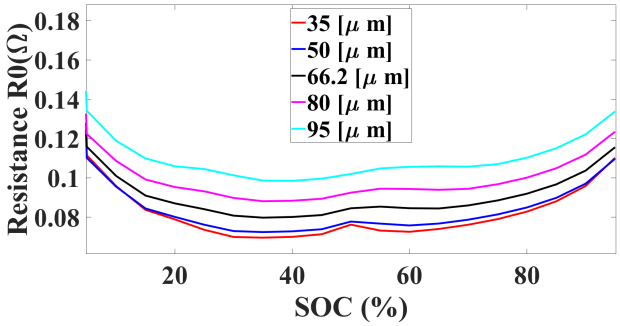

Figure 4.4: Value of R_0 for the SOC range 5 % to 95 % for the NMC-111 battery cell.

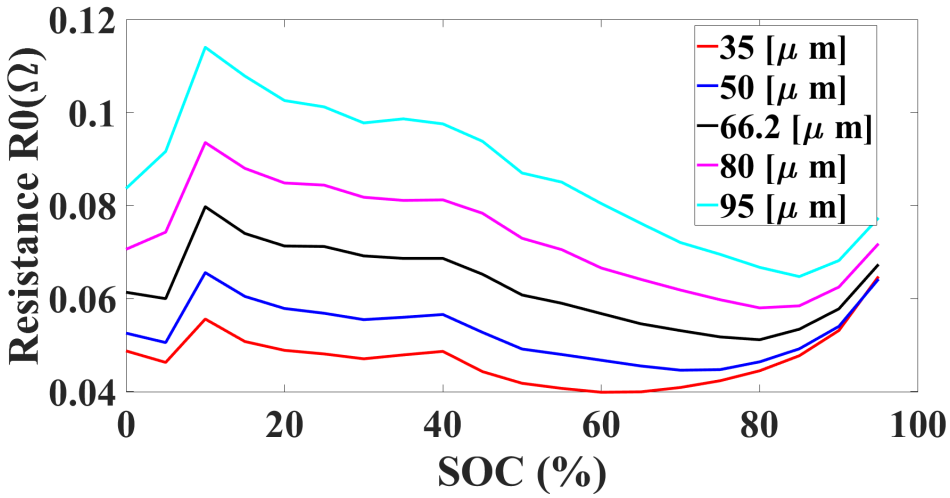

Figure 4.5: Value of R_0 for the entire SOC range for the LFP battery cell.

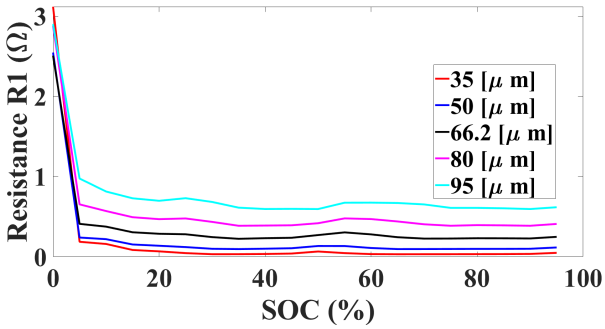

Figure 4.6: Value of R_1 for the entire SOC range for the NMC-811 battery cell.

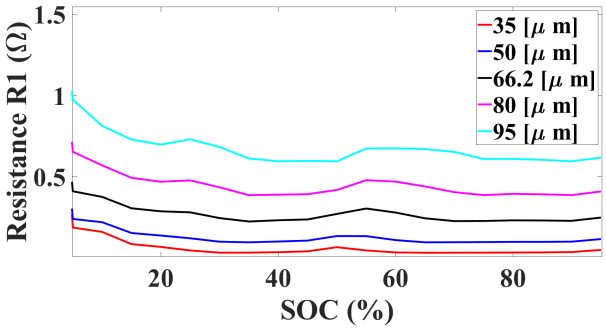

Figure 4.7: Value of R_1 for the SOC range 5 % to 95 % for the NMC-811 battery cell.

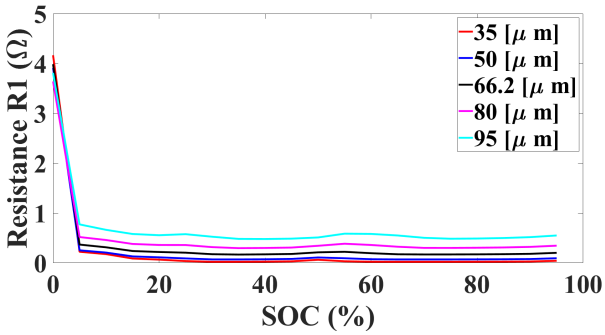

Figure 4.8: Value of R_1 for the entire SOC range for the NMC-111 battery cell.

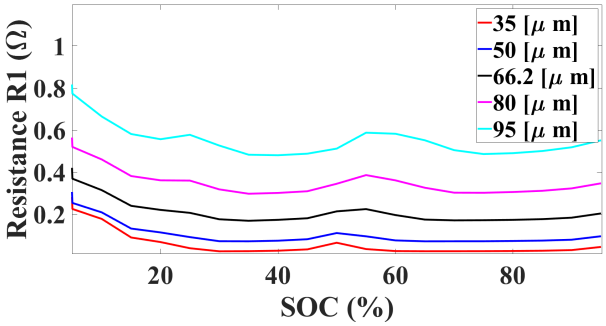

Figure 4.9: Value of R_1 for the SOC range 5 % to 95 % for the NMC-111 battery cell.

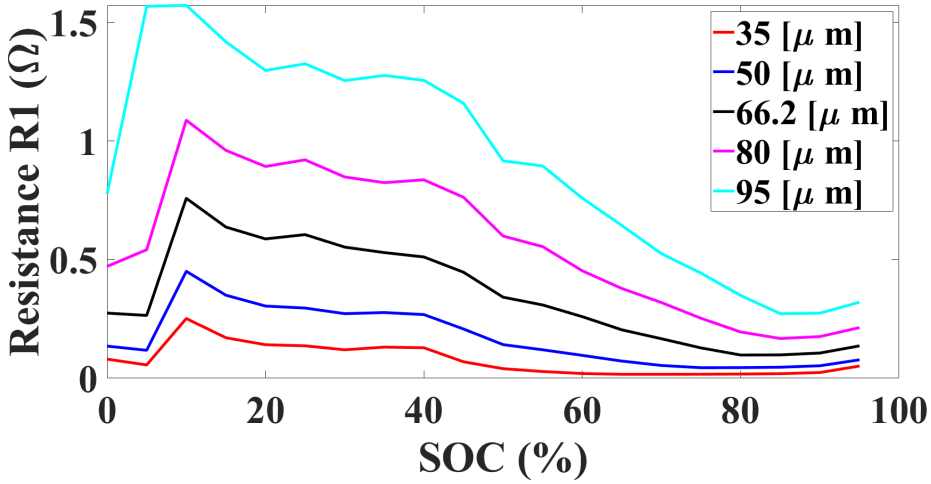

Figure 4.10: Value of R_1 for the entire SOC range for the LFP battery cell.

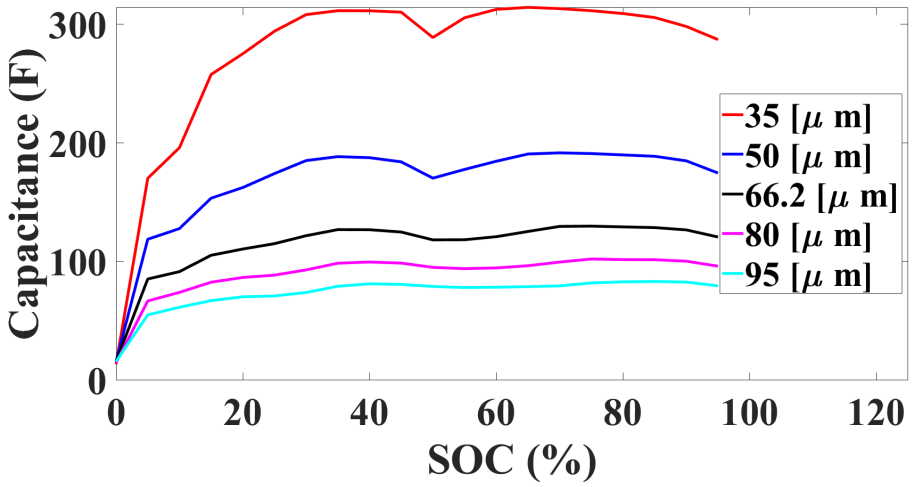

Figure 4.11: Value of C_1 for the entire SOC range for the NMC-811 battery cell.

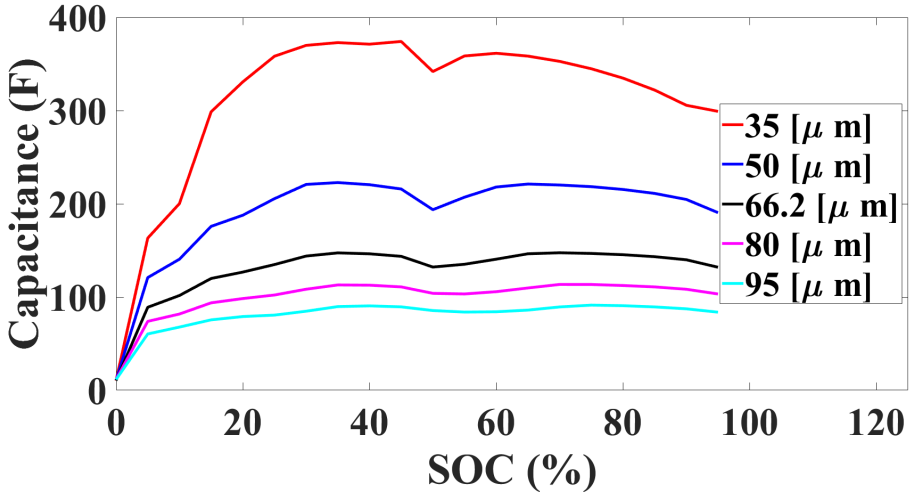

Figure 4.12: Value of C_1 for the entire SOC range for the NMC-111 battery cell.

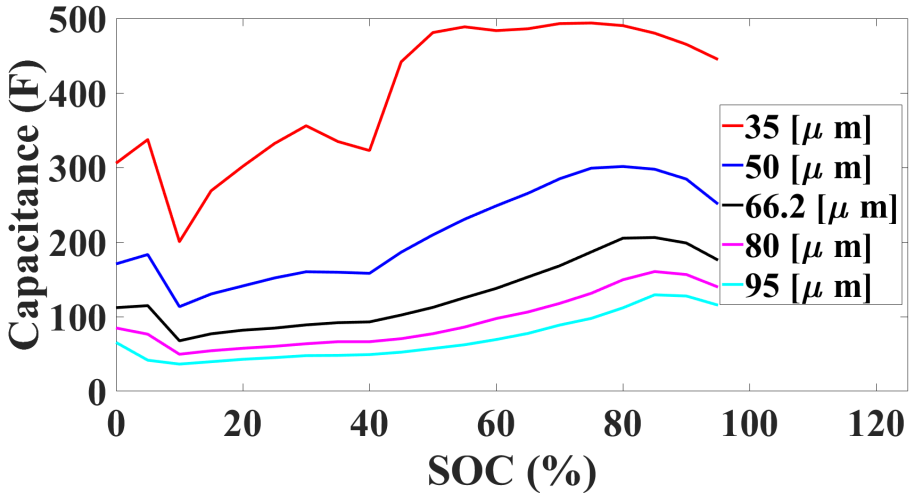

Figure 4.13: Value of C_1 for the entire SOC range for the LFP battery cell.

4.2 Energy Power Trade-off

The trade-off between energy density and power density for each cell chemistry is visualised in the ragone plots in figure 4.14 through 4.16. The arrows in these figures represents the iteration where the 1C simulation is used. From the figures it can be seen that the NMC-811 has both higher power and energy density than NMC-111 which in turn has higher power density and energy density than the LFP. The arrows indicates that the battery pack for the thicker cells requires the battery pack to be modelled after current densities lower than the 1C current density.

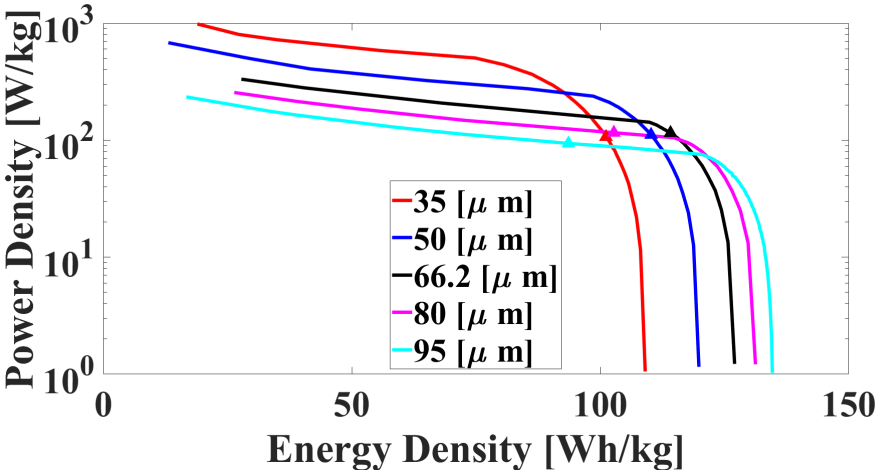

Figure 4.14: Ragone plot of the NMC-811 Chemistries, with the arrow representing the simulation instance of 1C

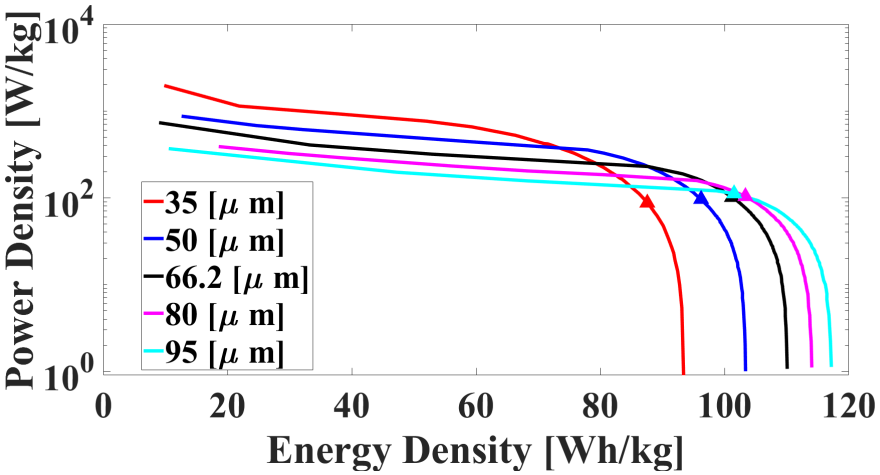

Figure 4.15: Ragone plot of the NMC-111 Chemistries, with the arrow representing the simulation instance of 1C

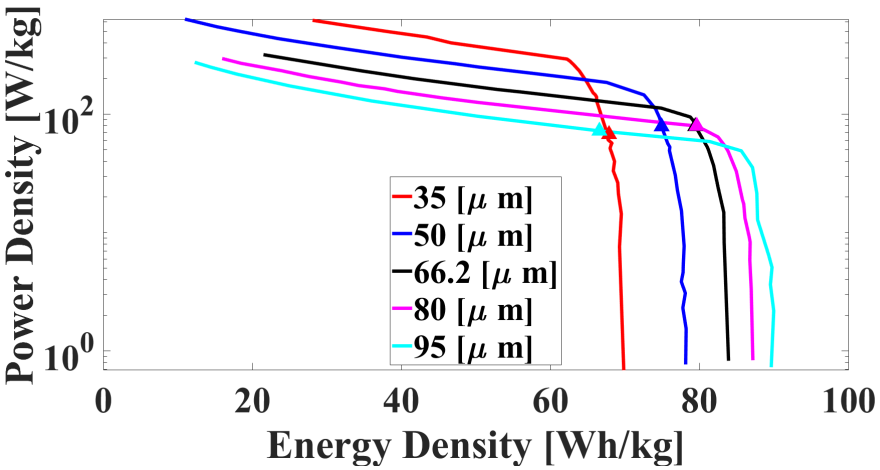

Figure 4.16: Ragone plot of the LFP Chemistries, with the arrow representing the simulation instance of 1C

In order to model the battery pack properly, the maximum usable capacity of each cell is required. Figure 4.17 through 4.19 shows the capacity of the cell in relation to the C-rate used for each simulation. The battery pack is modelled after the capacity before the steep decline of the figures. The capacity values chosen are displayed in table 4.1. As can be seen from table A.4 though A.6 in the appendix, the weight is minimal around the thickness of 66.2μm or all chemistries which is due to the trade-off between power density and energy density and as such the thicker cells need to increase the number to meet the power demand and the thinner cells need to increase the numbers to meet the energy demand.

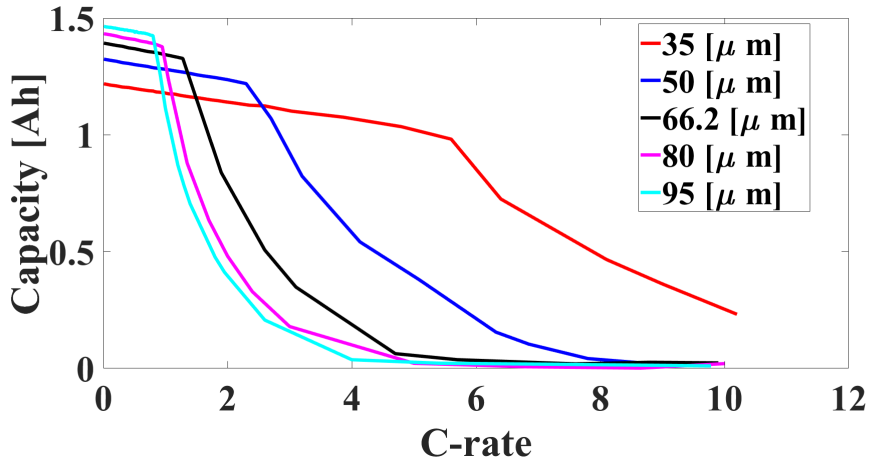

Figure 4.17: Capacity of the NMC-811 chemistry for varying C-rates.

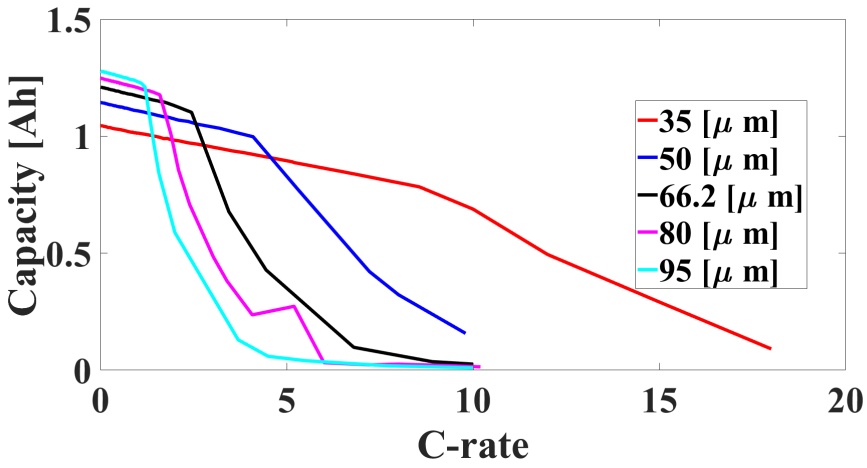

Figure 4.18: Capacity of the NMC-111 chemistry for varying C-rates.

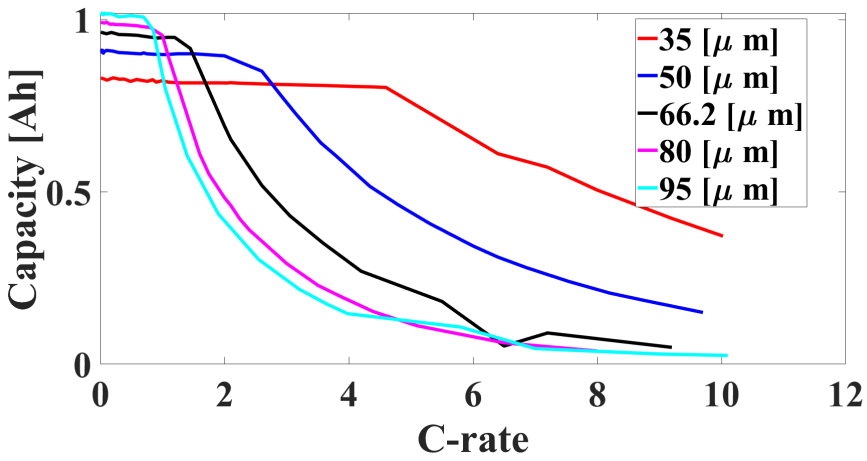

Figure 4.19: Capacity of the LFP chemistry for varying C-rates.

Table 4.1: Capacity of the different batteries.

Capacity [Ah]	NMC-811	NMC-111	LFP
$35\mu m$	1.0347	0.8868	0.8034
$50\mu m$	1.219	0.9974	0.8953
$66.2\mu m$	1.3269	1.1016	0.9167
$80\mu m$	1.3770	1.1763	0.9548
$95\mu m$	1.4245	1.2099	0.9709

4.3 Battery Specifications

The specifications regarding the batteries performance are displayed in this section. Information regarding the individual component contribution to the weight of the cells can be found in the appendix in table A.4 to A.6.

Table 4.2: Battery data for the NMC-811 chemistry

NMC-811	35[μm]	50[μm]	66.2[μm]	80[μm]	95[μm]
weight [kg]	319.2	288.2	278.3	292.4	333.6
Number of cells	7533	6882	6696	7068	8091
Energy [kWh]	32.22	35.56	34.14	36.11	37.78
Power [kW]	140.76	68.47	39.61	30.70	25.17
Capacity [Ah]	83.81	90.21	95.54	104.65	123.93

Table 4.3: Battery data for the NMC-111 chemistry

NMC-811	35[μm]	50[μm]	66.2[μm]	80[μm]	95[μm]
weight [kg]	381.4	329.7	311.6	311.2	313
Number of cells	8835	7719	7347	7371	7440
Energy [kWh]	32.5	33.7	33.44	35.20	36
Power [kW]	160.35	78.68	71.25	49.01	37.54
Capacity [Ah]	86.02	82.78	87.02	95.28	96.79

Table 4.4: Battery data for the LFP chemistry

NMC-811	35[μm]	50[μm]	66.2[μm]	80[μm]	95[μm]
weight [kg]	439.4	439	424	430.2	482.4
Number of cells	11155	11385	11155	11413	12880
Energy [kWh]	30.278	33.58	34.39	37.61	42.409
Power [kW]	128.52	67.62	47.79	34.21	28.37
Capacity [Ah]	77.93	88.63	88.92	96.43	108.74

4.4 Energy consumption

Due to the trade-off between energy and power optimized battery packs, the vehicles can travel different distances depending on the thickness of the electrodes. As such, to ensure proper comparison between the different batteries, the energy losses will be analysed as the energy loss per kilometer travelled. The losses of the ECM circuit are displayed in figure 4.20 as the percentage of the OCV energy output dissipated by the individual ECM parameters per kilometer travelled. The values used to visualise the simulation is displayed in the appendix in table A.1 through A.3.

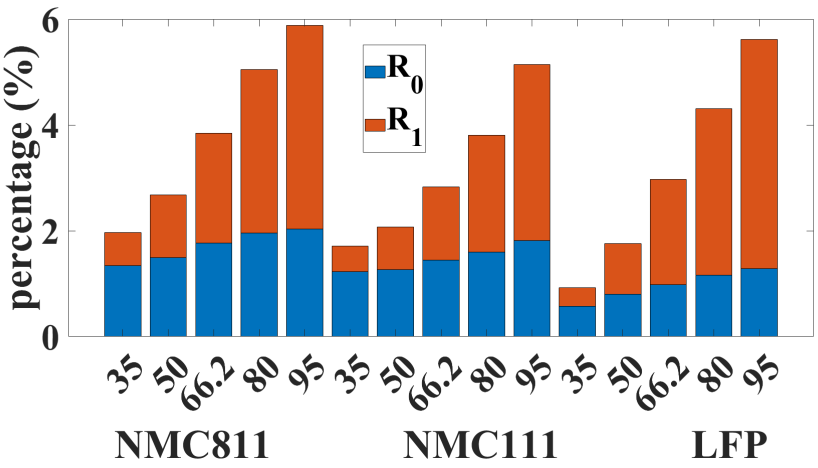

Figure 4.20: The percentage of energy from the OCV source dissipated by the ECM parameters

As previously discussed, the resistance values of R_0 and R_1 increases with the increase of thickness and, thus, the total losses will increase as the thickness increases. The NMC-811 battery exudes higher losses than the NMC-111 for each thickness and the LFP has lower losses than the other two for lower thicknesses but higher losses than NMC-111 at higher thicknesses.

4.4.1 Low SOC losses

In order to analyse the losses for the low SOC range of the cells, a constant power was applied to the battery pack for the low SOC range. The power had a low value of 5000 Watt, which was chosen due to the power output not being able to produce enough power to compensate for the high losses at higher input power values. The efficiency for the different chemistries and thickness for the low SOC range of 5% to 0% are displayed in figure 4.21 through 4.23.

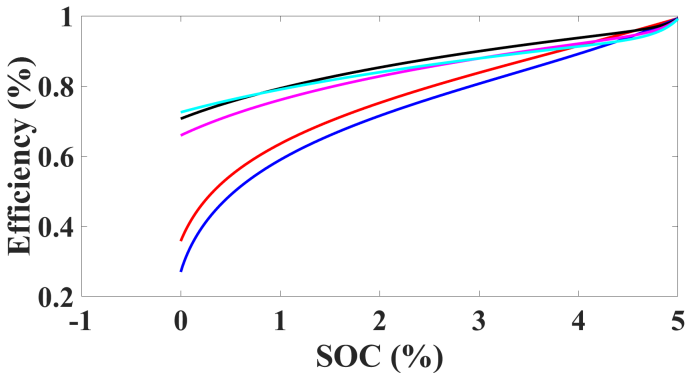

Figure 4.21: The efficiency of the different thicknesses for the SOC range of 5 to 0 % for NMC-811.

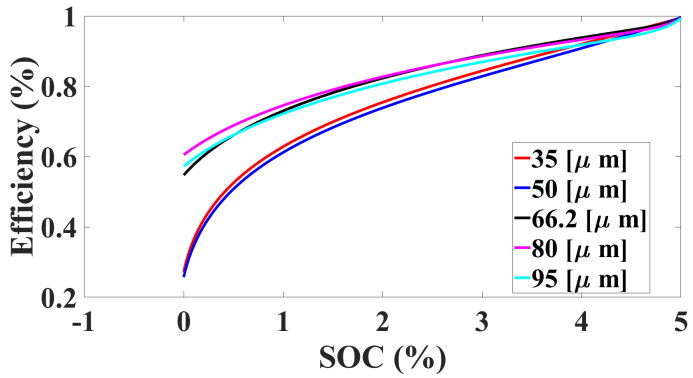

Figure 4.22: The efficiency of the different thicknesses for the SOC range of 5 to 0 % for NMC-111.

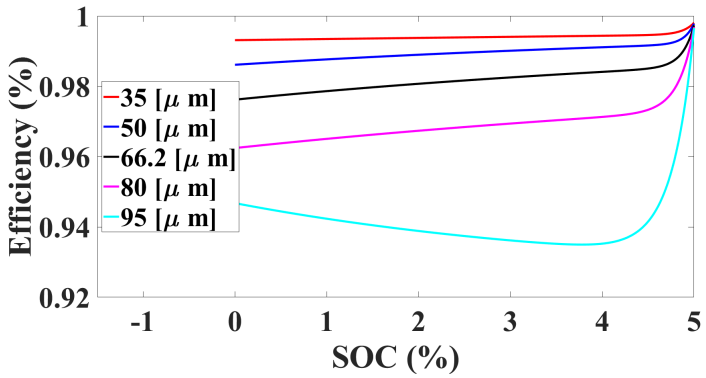

Figure 4.23: The efficiency of the different thicknesses for the SOC range of 5 to 0 % for LFP.

The drastic decrease in efficiency for the low SOC range for the NMC-811 and NMC-111 chemistry is indicative that this SOC range should be avoided during cycling. LFP has much better performance during this SOC range as it is similar to the losses experienced at the higher SOC range of 100% to 5%.

4.4.2 GHG emissions during cycling

The GHG emissions of EVs during cycling are based on the emissions from energy production and thus, different countries has different emissions during cycling. In this thesis, two countries energy mix is introduced: Sweden's Energy mix at 40 gCO_2/kWh and South Korea's energy mix at 690 gCO_2/kWh providing a low emissions and a high emissions scenario. The GHG emissions will be analysed as GHG emissions per kilometer travelled. These two cases will be performed for both the Swedish and Korean energy mixes. The data used for the losses is available in tables A.1 through A.3 in the appendix. The emissions can be viewed in figure 4.24 with the Swedish energy mix in the left y-axis and the South Korean energy mix in

the right y-axis. The emissions data for the Swedish energy mix and South Korean energy mix is available in the appendix in table A.13 and table A.15 vice versa.

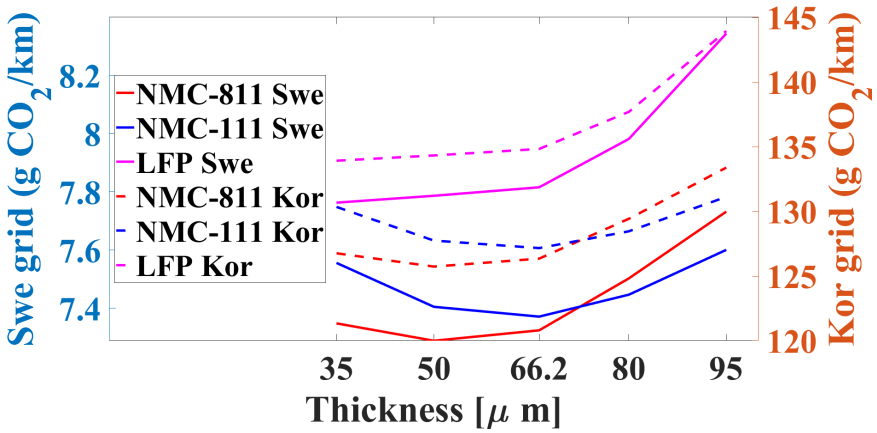

Figure 4.24: Total emissions per km travelled, the left axis represents the emissions based on the Swedish grid and the right axis represents the losses for the South korean grid.

The losses of the battery contributes to the emission of greenhouse gas and to be able to analyze the amount of emissions contributed to the losses, the same analysis is performed but only for the percentage attributed to the losses. The losses affects the battery both during charging and discharging of the battery and thus the losses of the battery will be doubled during this simulation. The result can be seen in figure 4.25 with the Swedish energy mix in the left y-axis and the South Korean energy mix in the right y-axis. Figure 4.26 represents the emissions caused by the energy that is not dissipated by the ECM parameters during cycling. The emissions data related to the losses for the Swedish energy mix and South Korean energy mix is available in the appendix in table A.14 and table A.16 vice versa.

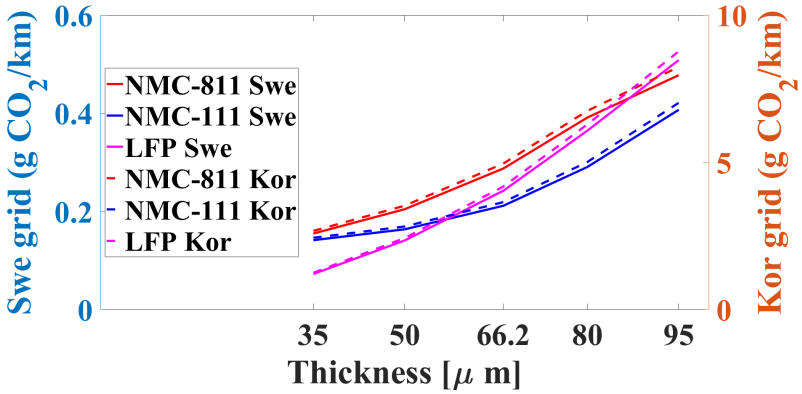

Figure 4.25: Total emissions per km travelled attributed to the losses, the left axis represents the emissions based on the Swedish grid and the right axis represents the losses for the South korean grid.

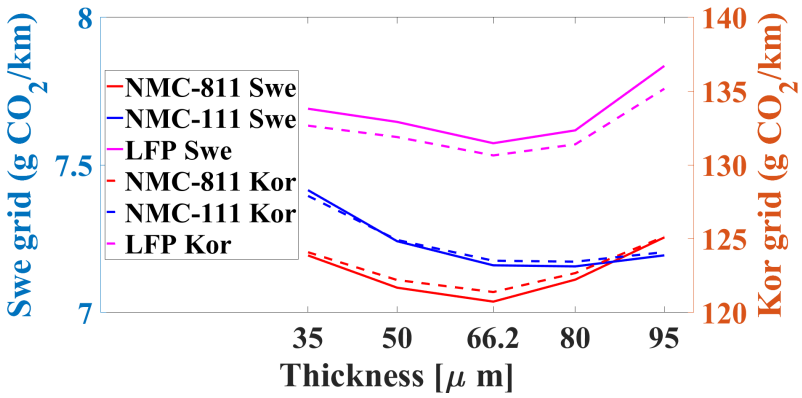

Figure 4.26: Total emissions per km travelled not attributed to the losses, the left axis represents the emissions based on the Swedish grid and the right axis represents the losses for the South korean grid.

Figure 4.24 indicates that the NMC-811 chemistry with cathode thickness of $50\mu m$ is superior during cycling. Figure 4.26 shows that the thickness of $66.2\mu m$ requires less energy to cycle and thus has lower emissions for all chemistries when not considering the energy dissipated in the ECM parameters. By analysing figure 4.25 it is clear that the emissions from the energy dissipated in the ECM parameters is lower for smaller electrode thicknesses. Thus, the optimal choice of cell is the NMC-811 with a thickness of $50\mu m$ as the decrease in energy losses by lowering the thickness is enough to warrant a choice of a smaller thickness than $66.2\mu m$.

4.5 Environmental and cost analysis

The contributions of each individual cell component to the weight can be be found in the appendix in table A.8 through A.10. Figure 4.27 and 4.28 shows the environmental impact and economical cost respectively, based on electrode thickness and battery pack weight. The individual component contribution to the weight is displayed in the appendix in table A.4 through A.6. The individual contribution of each component is also displayed in the appendix, table A.7 through A.9 for the environmental contributions and table A.10 through A.12 for the cost contributions.

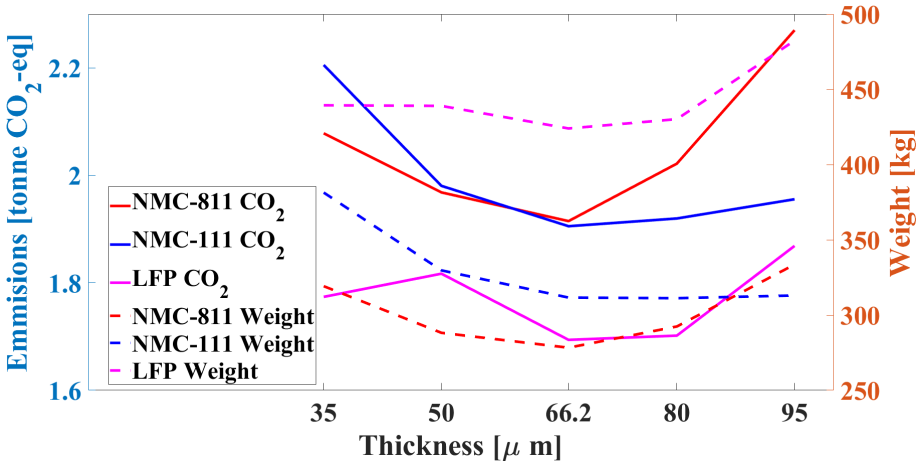

Figure 4.27: The GHG emmisions of the different battery chemistries and thicknesses displayed on the left y-axis and the weight of the batteries displayed on the right y-axis, with the whole lines representing the Cost and the dashed lines represent the weight.

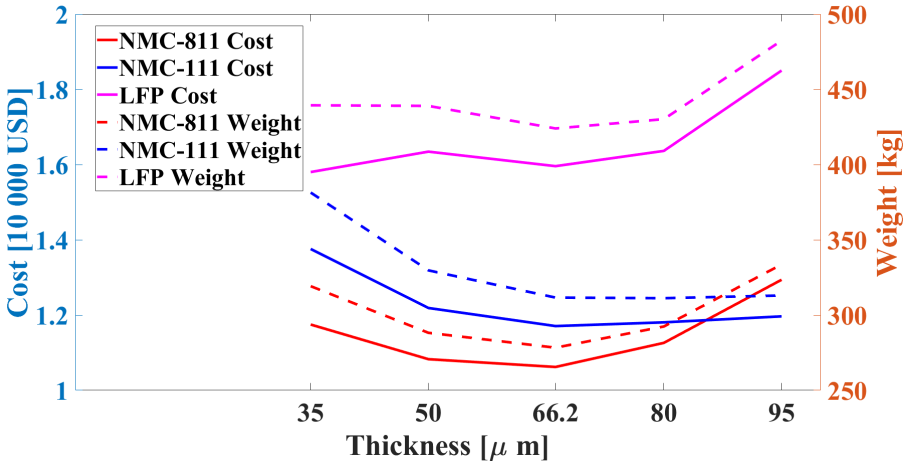

Figure 4.28: The financial cost of the different battery chemistries and thicknesses displayed on the left y-axis and the weight of the batteries displayed on the right y-axis, with the whole lines representing the cost and the dashed lines represent the weight.

As can be seen in figure 4.27 and 4.28 the optimal choice for all three chemistries is the cell thickness of 66.2μm. The $NMC811$ cathode chemistry is shown to be superior from an economical standpoint however not from an environmental standpoint. The NMC811 has a higher nickel concentration and thus has higher average emissions than the NMC111 cathode, however, these emission differences at not that high at the 66.2μm thickness. The LFP Battery packs displays the lowest emissions even though the number of cells are higher, which is due to the relatively low emissions of the cathode chemistry in relation to the other cells. The cost of the LFP

cell is much higher than the cost of both the NMC chemistries, which is due to the increased number of cells needed to be manufactured. The battery assembly is the main cost for all cells and thus the number of cells in a battery pack greatly determines the price of the pack.

4.6 Comparison of Assembly and Performance

The battery pack with least emissions during cycling was the NMC-811 cell with a thickness of $50\mu m$ and the cell with least emissions during the assembly process was the LFP cell with a thickness of $66.2\mu m$. The emissions for this NMC-811 cell during cycling is $7.2887[gCO_2eq/km]$ and $125.73[gCO_2eq/km]$ for the Swedish and South Korean Energy mix separately. For the previously named LFP cell the emissions during cycling is $7.8159[gCO_2eq/km]$ and $134.82[gCO_2eq/km]$ for the Swedish and South Korean Energy mix separately. The NMC-811 cell thus produces $0.5272[gCO_2eq/km]$ and $9.09[gCO_2eq/km]$ less per cycle than the LFP cell for the Swedish and South Korean Energy mix separately. The production of the LFP cell creates GHG emissions of $1693.8[kgCO_2eq]$ and the production of the NMC-811 cell creates GHG emissions of $1968.2[kgCO_2eq]$. Thus the NMC-811 cell needs to mitigate $274.4[kgCO_2eq]$ during cycling in order to be better than the LFP cell from a climate perspective. Using the Swedish energy mix the distance required for the NMC-811 to outperform the LFP is 520490 kilometers and for the South Korean energy mix 30187 kilometers is required. Each cycle is considered to be 370 kilometers, and thus, the total amount of cycles needed for the NMC-811 to outperform the LFP is 1406 cycles for the Swedish energy mix and 82 cycles for the South Korean energy mix. This indicates that the LFP is more optimal from an environmental perspective for countries that already sustain low GHG emissions during their energy production and that the NMC-811 is optimal in a country with higher GHG emissions during production.

5
Conclusion

5.1 Discussion

The analysis shows that the efficiency of the cell increases as thickness decreases and that the efficiency increase when lowering the thickness from the thickness representing the optimal weight based, can provide less GHG emissions. It was also indicated that the optimal choice of cell chemistry is very much dependant on the GHG emissions of the power production used to charge the electric vehicle. From an environmental perspective NMC-111 always performed worse than both LFP and NMC-811 as the low emissions from manufacturing of the LFP was always lower than NMC-111 and the NMC-811 and NMC-811 had lower emissions during cycling than both NMC-111 and LFP. Two of the most important aspects for a consumer when deciding to switch from a fuel based vehicle to an electric vehicle is the cost and range of the vehicle. This can be a limiting factor when considering the LFP chemistry as it has the lowest energy and power density of the three chemistries, which results in a higher number of batteries to compensate. The number of batteries in a battery pack impacts the price much more than the cost of the materials due to the high manufacturing cost. The NMC-811 is therefore a really attractive battery chemistry as the increased energy density, and thus lower amount of cells, compensates for the higher price of the cathode material compared to the NMC-111 and LFP cells. The diminishing cobalt resources in the world will however increase the cost of NMC-111 and NMC-811 as time continues. The LFP was chosen for investigation due to its lack of cobalt and the generally more inexpensive and environmentally friendly material.

5.2 Answers to Research Questions

How does the thickness of the electrodes affect the performance of the battery?.
It is shown that the ECM parameters has very little impact on the battery performance in general as all batteries has above 99.7% efficiency. However, smaller thicknesses gave less losses for LFP during the entire SOC range, and less losses for NMC-811 and NMC-111 in the SOC range of 100 to 5% with a big increase in losses after this point.

How does the battery design impact the sizing of the battery pack in a vehicle application?
The power and energy requirements of the battery pack creates a trade off due to

the low energy density of the thin electrodes and the low power density of the thick electrodes. The optimal battery pack sizing is thus based on the thickness where the trade-off between power density and energy density is as small as possible.

What is the environmental impact of the different battery packs and cell designs? It is shown that the LFP chemistry has the lowest manufacturing emissions but that the NMC-811 chemistry has the lowest cycling emissions and that the optimal choice of battery design depends on how many times the battery pack can be cycled and the GHG emissions from the power production of the country.

What is the economical impact of the different battery packs and cell designs? The cost was shown to be heavily related to the number of cells and thus the chemistry with the higher energy density performed best, thus the optimal cell is the NMC-811 with an optimised ratio between power and energy density.

5.3 Ethics

The battery industry today is heavily reliant on cobalt, which is a very controversial subject as the extraction of the cobalt is linked to child labour. Cobalt is also a diminishing resource which implies that the price will increase, possibly leading to conflicts over the material. The most prominent alternative to cobalt based materials in the industry today is the LFP chemistry. The LFP chemistry also shows promise due to its low emissions during production, however, the change from NMC-811 which is the most prominent chemistry today to the LFP chemistry comes with a cost increase of several thousands of dollars for each battery pack. Switching from NMC-811 to LFP might therefore come with a big financial risk to the vehicle manufacturers due to the increased production cost and fewer customers since they have to increase the price of the vehicle.

5.4 Future work

The simulations for this thesis were performed under ideal conditions, with a constant temperature and no aging present in the cells. The next step to further research this subject is to investigate how the losses change with temperature and increased age. While performing an aging test, investigation could also be included into the effects of aging on the environmental aspects i.e investigating the GHG emissions related to how many cycles can be performed for the cell. How the battery could be repurposed at end of its life and the environmental aspects related to that would also be interesting to investigate. Future research could also include researching how other anode materials would affect the performance of the cell i.e silicon.

The major cost of the battery production came from the per unit cost of the cell, therefore it would be interesting to increase the size of each cell in order to see how the cost would change. The environmental and cost analysis were performed with data obtained from pre-existing data bases, it would however be interesting

to perform a thorough life cycle analysis from both an economic and environmental aspect.

Bibliography

[1] J. Newman and W. Tiedemann, "Porous-electrode theory with battery applications," *AIChE Journal*, vol. 21, no. 1, pp. 25–41, 1975.

[2] M. Doyle, T. F. Fuller, and J. Newman, "Modeling of galvanostatic charge and discharge of the lithium/polymer/insertion cell," *Journal of the Electrochemical society*, vol. 140, no. 6, p. 1526, 1993.

[3] T. F. Fuller, M. Doyle, and J. Newman, "Simulation and optimization of the dual lithium ion insertion cell," *Journal of the Electrochemical Society*, vol. 141, no. 1, p. 1, 1994.

[4] T. Hofman and C. Dai, "Energy efficiency analysis and comparison of transmission technologies for an electric vehicle," in *2010 IEEE vehicle power and propulsion conference*, IEEE, 2010, pp. 1–6.

[5] A. Latz, J. Zausch, and O. Iliev, "Modeling of species and charge transport in li–ion batteries based on non-equilibrium thermodynamics," in *International Conference on Numerical Methods and Applications*, Springer, 2010, pp. 329–337.

[6] T.-S. Dao, C. P. Vyasarayani, and J. McPhee, "Simplification and order reduction of lithium-ion battery model based on porous-electrode theory," *Journal of Power Sources*, vol. 198, pp. 329–337, 2012.

[7] F. J. Vidal-Iglesias, J. Solla-Gullón, A. Rodes, E. Herrero, and A. Aldaz, "Understanding the nernst equation and other electrochemical concepts: An easy experimental approach for students," *Journal of Chemical Education*, vol. 89, no. 7, pp. 936–939, 2012.

[8] H. Zheng, J. Li, X. Song, G. Liu, and V. S. Battaglia, "A comprehensive understanding of electrode thickness effects on the electrochemical performances of li-ion battery cathodes," *Electrochimica Acta*, vol. 71, pp. 258–265, 2012.

[9] O. E. Bankole, C. Gong, and L. Lei, "Battery recycling technologies: Recycling waste lithium ion batteries with the impact on the environment in-view," *Journal of Environment and Ecology*, vol. 4, p. 14, Jun. 2013. DOI: 10.5296/jee.v4i1.3257.

[10] R. J. Brodd and C. Helou, "Cost comparison of producing high-performance li-ion batteries in the us and in china," *Journal of Power Sources*, vol. 231, pp. 293–300, 2013.

[11] L. W. Yao, J. A. Aziz, P. Y. Kong, and N. R. N. Idris, "Modeling of lithium-ion battery using matlab/simulink," in *IECON 2013-39th Annual Conference of the IEEE Industrial Electronics Society*, IEEE, 2013, pp. 1729–1734.

[12] G. André and M. Godin, "Child labour, agency and family dynamics: The case of mining in katanga (drc)," *Childhood*, vol. 21, no. 2, pp. 161–174, 2014.

[13] H. Berg, *Batteries for electric vehicles: materials and electrochemistry*. Cambridge university press, 2015.

[14] C.-S. Kim, K. M. Jeong, K. Kim, and C.-W. Yi, "Effects of capacity ratios between anode and cathode on electrochemical properties for lithium polymer batteries," *Electrochimica Acta*, vol. 155, pp. 431–436, 2015.

[15] A. Ramos and C. Please, "Some comments on the butler-volmer equation for modeling lithium-ion batteries," *arXiv preprint arXiv:1503.05912*, 2015.

[16] M. Singh, J. Kaiser, and H. Hahn, "Thick electrodes for high energy lithium ion batteries," *Journal of The Electrochemical Society*, vol. 162, no. 7, A1196, 2015.

[17] S. J. An, J. Li, C. Daniel, D. Mohanty, S. Nagpure, and D. L. Wood III, "The state of understanding of the lithium-ion-battery graphite solid electrolyte interphase (sei) and its relationship to formation cycling," *Carbon*, vol. 105, pp. 52–76, 2016.

[18] E. A. Grunditz, *Design and assessment of battery electric vehicle powertrain, with respect to performance, energy consumption and electric motor thermal capability*. Chalmers Tekniska Hogskola (Sweden), 2016.

[19] E. A. Grunditz and T. Thiringer, "Performance analysis of current bevs based on a comprehensive review of specifications," *IEEE Transactions on Transportation Electrification*, vol. 2, no. 3, pp. 270–289, 2016.

[20] K. Itani, A. De Bernardinis, Z. Khatir, and A. Jammal, "Integration of different modules of an electric vehicle powered by a battery-flywheel storage system during traction operation," in *2016 IEEE International Multidisciplinary Conference on Engineering Technology (IMCET)*, IEEE, 2016, pp. 126–131.

[21] T. Satyavani, B. R. Kiran, V. R. Kumar, A. S. Kumar, and S. Naidu, "Effect of particle size on dc conductivity, activation energy and diffusion coefficient of lithium iron phosphate in li-ion cells," *Engineering Science and Technology, an International Journal*, vol. 19, no. 1, pp. 40–44, 2016.

[22] R. Jung, M. Metzger, F. Maglia, C. Stinner, and H. A. Gasteiger, "Oxygen release and its effect on the cycling stability of linixmnycozo2 (nmc) cathode materials for li-ion batteries," *Journal of The Electrochemical Society*, vol. 164, no. 7, A1361, 2017.

[23] B. Świeczko-Żurek, P. Jaskula, J. A. Ejsmont, A. Kędzierska, and P. Czajkowski, "Rolling resistance and tyre/road noise on rubberised asphalt pavement in poland," *Road Materials and Pavement Design*, vol. 18, no. 1, pp. 151–167, 2017.

[24] E. Wikner, *Lithium ion battery aging: battery lifetime testing and physics-based modeling for electric vehicle applications*. Chalmers Tekniska Hogskola (Sweden), 2017.

[25] P. Alves Dias, D. Blagoeva, C. Pavel, and N. Arvanitidis, "Cobalt: Demand-supply balances in the transition to electric mobility," *European Commission, Joint Research Centre, EUR-Scientific and Technical Research Reports Publications Office of the European Union*, vol. 10, p. 97 710, 2018.

[26] L. Chen, Z. Chen, S. Liu, B. Gao, and J. Wang, "Effects of particle size distribution on compacted density of lithium iron phosphate 18650 battery," *Journal of Electrochemical Energy Conversion and Storage*, vol. 15, no. 4, 2018.

[27] G. Deal, "Communication from the commission to the european parliament, the european council, the council, the european economic and social committee and the committee of the regions," 2018.

[28] M. Hossain, S. Saha, M. E. Haque, M. T. Arif, and A. M. T. Oo, "A parameter extraction method for the thevenin equivalent circuit model of li-ion batteries," in *2019 IEEE Industry Applications Society Annual Meeting*, IEEE, 2019, pp. 1–7.

[29] M. Raugei and P. Winfield, "Prospective lca of the production and eol recycling of a novel type of li-ion battery for electric vehicles," *Journal of Cleaner Production*, vol. 213, pp. 926–932, 2019.

[30] J. Sturm, A. Rheinfeld, I. Zilberman, F. B. Spingler, S. Kosch, F. Frie, and A. Jossen, "Modeling and simulation of inhomogeneities in a 18650 nickel-rich, silicon-graphite lithium-ion cell during fast charging," *Journal of Power Sources*, vol. 412, pp. 204–223, 2019.

[31] M. Xu, B. Reichman, and X. Wang, "Modeling the effect of electrode thickness on the performance of lithium-ion batteries with experimental validation," *Energy*, vol. 186, p. 115 864, 2019.

[32] C. Aichberger and G. Jungmeier, "Environmental life cycle impacts of automotive batteries based on a literature review," *Energies*, vol. 13, no. 23, p. 6345, 2020.

[33] S. W. D. Gourley, T. Or, and Z. Chen, "Breaking free from cobalt reliance in lithium-ion batteries," *Iscience*, vol. 23, no. 9, p. 101 505, 2020.

[34] M. Sheikh, A. Elmarakbi, and S. Rehman, "A combined experimental and simulation approach for short circuit prediction of 18650 lithium-ion battery under mechanical abuse conditions," *Journal of Energy Storage*, vol. 32, p. 101 833, 2020.

[35] F. Wang, Y. Deng, and C. Yuan, "Life cycle assessment of lithium oxygen battery for electric vehicles," *Journal of Cleaner Production*, vol. 264, p. 121 339, 2020.

[36] M. Chordia, A. Nordelöf, and L. A.-W. Ellingsen, "Environmental life cycle implications of upscaling lithium-ion battery production," *The International Journal of Life Cycle Assessment*, vol. 26, no. 10, pp. 2024–2039, 2021.

[37] M.-K. Tran, A. DaCosta, A. Mevawalla, S. Panchal, and M. Fowler, "Comparative study of equivalent circuit models performance in four common lithium-ion batteries: Lfp, nmc, lmo, nca," *Batteries*, vol. 7, no. 3, p. 51, 2021.

[38] M. Yu, B. Bai, S. Xiong, and X. Liao, "Evaluating environmental impacts and economic performance of remanufacturing electric vehicle lithium-ion batteries," *Journal of Cleaner Production*, vol. 321, p. 128 935, 2021.

[39] (), [Online]. Available: https://www.li-polymer-battery.com/.

[40] Bentley. (). "Coming this way: The electric bentley," [Online]. Available: https://www.bentleymotors.com/en/world-of-bentley/beyond-100/the-electric-bentley.html. (accessed:2022.03.13).

[41] A. N. Laboratory. (). "The greenhouse gases, regulated emissions, and energy use in technologies model," [Online]. Available: https://greet.es.anl.gov.

[42] K. G. G. Paul A. Nelson, D. W. D. Shabbir Ahmed, I. D. B. Naresh Susarla, J. S. Joseph J. Kubal, and Z. Liu. (). "Batpac model software," [Online]. Available: https://www.anl.gov/cse/batpac-model-software.

[43] UNECE. (). "Un regulation no. 154 - worldwide harmonized light vehicles test procedure (wltp)," [Online]. Available: https://unece.org/transport/documents/2021/02/standards/un-regulation-no-154-worldwide-harmonized-light-vehicles-test.

[44] Volvo. (). "Volvo cars to be fully electric by 2030," [Online]. Available: https://www.media.volvocars.com/global/en-gb/media/pressreleases/277409/volvo-cars-to-be-fully-electric-by-2030. (accessed:2022.03.13).

[45] E. Zurich. (). "The qss toolbox manual," [Online]. Available: https://idsc.ethz.ch/research-guzzella-onder/downloads.html. (accessed:2022.01.20).

A

Appendix 1

Table A.1: Energy consumption of NMC-811 battery

NMC-811	35[μm]	50[μm]	66.2[μm]	80[μm]	95[μm]
Distance [km]	378.2	381.1	379.2	382.6	388.6
Energy output of OCV [kWh]	69.5	69.5	69.4	71.7	75.1
OCV Energy per kilometer [Wh/km]	183.7	182.2	183.1	187.6	193.3
Total parameter loss per kilometers [Wh/km]	3.8788	5.1185	7.1927	9.7897	11.9469
R0 energy losses per kilometer [Wh/km]	2.4589	2.7216	3.2309	3.6662	3.9352
R1 energy losses per kilometer [Wh/km]	1.1506	2.1510	3.8151	5.7925	7.4327
Efficiency [%]	97.89	97.19	96.07	94.78	93.82

Table A.2: Energy consumption of NMC-111 battery

NMC-111	35[μm]	50[μm]	66.2[μm]	80[μm]	95[μm]
Distance [km]	379.2	382.6	380.8	384.6	382.9
Energy output of OCV [kWh]	71.6	70.8	70.2	71.6	72.8
OCV Energy per kilometer [Wh/km]	188.9	185.1	184.3	186.2	190
Total parameter loss per kilometers [Wh/km]	3.5405	4.0952	5.2944	7.2705	10.1838
R0 energy losses per kilometer [Wh/km]	2.3221	2.3507	2.6654	2.9813	3.4502
R1 energy losses per kilometer [Wh/km]	0.9166	1.4770	2.5475	4.0974	6.3140
Efficiency [%]	98.13	97.79	97.13	96.09	94.64

Table A.3: Energy consumption of LFP battery

LFP	35[μm]	50[μm]	66.2[μm]	80[μm]	95[μm]
Distance [km]	383.3	378.3	384.5	381.1	382.1
Energy output of OCV [kWh]	74.4	73.6	75.1	76.1	79.7
OCV Energy per kilometer [Wh/km]	194.1	194.7	195.4	199.5	208.6
Total parameter loss per kilometers [Wh/km]	1.8179	3.5264	6.0597	9.1216	12.7167
R0 energy losses per kilometer [Wh/km]	1.1173	1.5623	1.9246	2.3077	2.6709
R1 energy losses per kilometer [Wh/km]	0.6712	1.8620	3.8814	6.2939	9.0439
Efficiency [%]	99.06	98.19	96.90	95.43	93.90

Table A.4: Weight of the individual components of the NMC-811 battery pack

NMC-811	35[μm]	50[μm]	66.2[μm]	80[μm]	95[μm]
Total weight [kg]	319.2	288.2	278.3	292.4	333.6
Number of cells [-]	7533	6882	6696	7068	8091
Weigth Anode [kg]	25.9	25.7	26.4	28.6	33.5
Weight Cathode [kg]	57.1	55	56.3	61.1	71.5
Weigth Copper [kg]	42.9	29.8	23.1	20.7	20.4
Weight Aluminum [kg]	20.4	14.2	11	9.9	9.7
Weight Case [kg]	57.1	52.2	50.8	53.6	61.4
Weight Separator [kg]	10.6	7.3	5.7	5.1	5
Weight Electrolyte [kg]	12.7	11.6	11.2	11.8	13.5

Table A.5: Weight of the individual components of the NMC-111 battery pack

NMC-111	35[μm]	50[μm]	66.2[μm]	80[μm]	95[μm]
Total weight [kg]	381.4	329.7	311.6	311.2	313
Number of cells [-]	8835	7719	7347	7371	7440
Weigth Anode [kg]	26	24.9	25	25.9	26.8
Weight Cathode [kg]	69.2	66.2	66.7	69	71.3
Weigth Copper [kg]	54.8	36.7	27.9	23.9	20.8
Weight Aluminum [kg]	26.1	17.5	13.3	11.4	9.9
Weight Case [kg]	67	58.6	55.8	55.9	56.4
Weight Separator [kg]	13.5	9	6.9	5.9	5.1
Weight Electrolyte [kg]	14.8	12.9	12.2	12.2	12.3

Table A.6: Weight of the individual components of the LFP battery pack

LFP	35[μm]	50[μm]	66.2[μm]	80[μm]	95[μm]
Total weight [kg]	439.4	439	424	430.2	482.4
Number of cells [-]	11155	11385	11155	11413	12880
Weigth Anode [kg]	32.4	36.2	37.6	39.8	45.8
Weight Cathode [kg]	66.4	86.4	77	81.1	94
Weigth Copper [kg]	69.6	54.5	42.7	37.2	36.3
Weight Aluminum [kg]	33.2	26	20.3	17.7	17.3
Weight Case [kg]	84.6	86.4	84.6	86.6	97.7
Weight Separator [kg]	17.1	13.4	10.5	9.2	9
Weight Electrolyte [kg]	18.7	18.9	18.5	18.9	21.3

Table A.7: Emission contribution for each component of the NMC-811 batteries

Emission NMC-811	35[μm]	50[μm]	66.2[μm]	80[μm]	95[μm]
Anode [kg $C0_2 - eq$]	116.6	115.7	118.8	128.7	150.8
Cathode [kg $C0_2 - eq$]	923.3	889.4	910.4	988.0	1156.2
Copper [kg $C0_2 - eq$]	144.1	100.1	77.6	69.6	68.5
Aluminum [kg $C0_2 - eq$]	158.7	110.5	85.6	77	75.5
Case [kg $C0_2 - eq$]	157	143.6	139.7	147.4	168.9
Separator [kg $C0_2 - eq$]	21.2	14.6	11.4	10.2	10
Electrolyte [kg $C0_2 - eq$]	121.9	111.4	107.5	113.3	129.6
Assembly [kg $C0_2 - eq$]	435.4	483.1	463.8	487.6	510.7
total [kg $C0_2 - eq$]	2078.3	1968.2	1914.8	2021.7	2270.1

Table A.8: Emission contribution for each component of the of NMC-111 batteries

Emission NMC-111	35[μm]	50[μm]	66.2[μm]	80[μm]	95[μm]
Anode [kg $C0_2 - eq$]	117	112.1	112.5	116.6	120.6
Cathode [kg $C0_2 - eq$]	891.3	852.7	859.1	888.7	918.3
Copper [kg $C0_2 - eq$]	184.1	123.3	93.7	80.3	69.9
Aluminum [kg $C0_2 - eq$]	203.1	136.2	103.5	88.7	77
Case [kg $C0_2 - eq$]	184.3	161.2	153.5	153.7	155.1
Separator [kg $C0_2 - eq$]	27	18	13.8	11.8	10.2
Electrolyte [kg $C0_2 - eq$]	142.1	123.8	117.1	117.1	118.1
Assembly [kg $C0_2 - eq$]	456.5	453.3	452.1	462.8	486.3
total [kg $C0_2 - eq$]	2205.3	1980.4	1905.3	1919.7	1955.5

Table A.9: Emission contribution for each component of the LFP batteries

Emission LFP	35[μm]	50[μm]	66.2[μm]	80[μm]	95[μm]
Anode [kg $C0_2 - eq$]	145.8	162.9	169.2	179.1	206.1
Cathode [kg $C0_2 - eq$]	284.2	369.8	329.6	347.1	402.3
Copper [kg $C0_2 - eq$]	233.9	183.1	143.5	125.0	122.0
Aluminum [kg $C0_2 - eq$]	258.3	202.3	157.9	137.7	134.6
Case [kg $C0_2 - eq$]	232.7	237.6	232.7	238.2	268.7
Separator [kg $C0_2 - eq$]	34.2	26.8	21	18.4	18
Electrolyte [kg $C0_2 - eq$]	179.5	181.4	177.6	181.4	204.5
Assembly [kg $C0_2 - eq$]	405.3	453.1	462.4	474.8	512.5
total [kg $C0_2 - eq$]	1773.8	1817.0	1693.8	1701.7	1868.7

Table A.10: Cost for each component of the NMC-811 batteries

cost NMC-811	35[μm]	50[μm]	66.2[μm]	80[μm]	95[μm]
Anode [USD]	259	257	264	286	335
Cathode [USD]	1484.6	1430	1463.8	1588.6	1859
Copper [USD]	32.2	29.5	28.7	30.3	34.6
Aluminum [USD]	5.4	4.9	4.8	5.0	5.8
Case [USD]	139.9	127.9	124.5	131.3	150.4
Separator [USD]	24.2	22.1	21.5	22.7	26.0
Electrolyte [USD]	84.7	77.3	74.7	78.7	90
Assembly [USD]	9717.6	8877.8	8637.8	9117.7	10437.0
total [USD]	11748	10826	10620	11260	12938

Table A.11: Cost contribution for each component of the NMC-111 batteries

cost NMC-111	35[μm]	50[μm]	66.2[μm]	80[μm]	95[μm]
Anode [USD]	260	249	250	259	268
Cathode [USD]	1764.6	1688.1	1700.9	1759.5	1818.1
Copper [USD]	37.8	33.0	31.5	31.6	31.8
Aluminum [USD]	6.3	5.5	5.2	5.3	5.3
Case [USD]	164.2	143.6	136.7	137.0	138.2
Separator [USD]	28.4	24.8	23.6	23.7	23.9
Electrolyte [USD]	98.7	86	81.3	81.3	82
Assembly [USD]	11397	9957.5	9477.6	9508.6	9597.6
total [USD]	13757	12188	11707	11806	11965

Table A.12: Cost contribution for each component of the LFP batteries

cost LFP [USD]	35[μm]	50[μm]	66.2[μm]	80[μm]	95[μm]
Anode [USD]	324	362	376	398	458
Cathode [USD]	664	864	770	811	940
Copper [USD]	47.7	48.7	47.7	48.9	55.1
Aluminum [USD]	8	8.1	8	8.1	9.2
Case [USD]	207.3	211.7	207.3	212.2	239.4
Separator [USD]	35.8	36.5	35.8	36.6	41.3
Electrolyte [USD]	124.7	126	123.3	126	142
Assembly [USD]	14390	14687	14390	14723	16615
total [USD]	15801	16344	15958	16364	18500

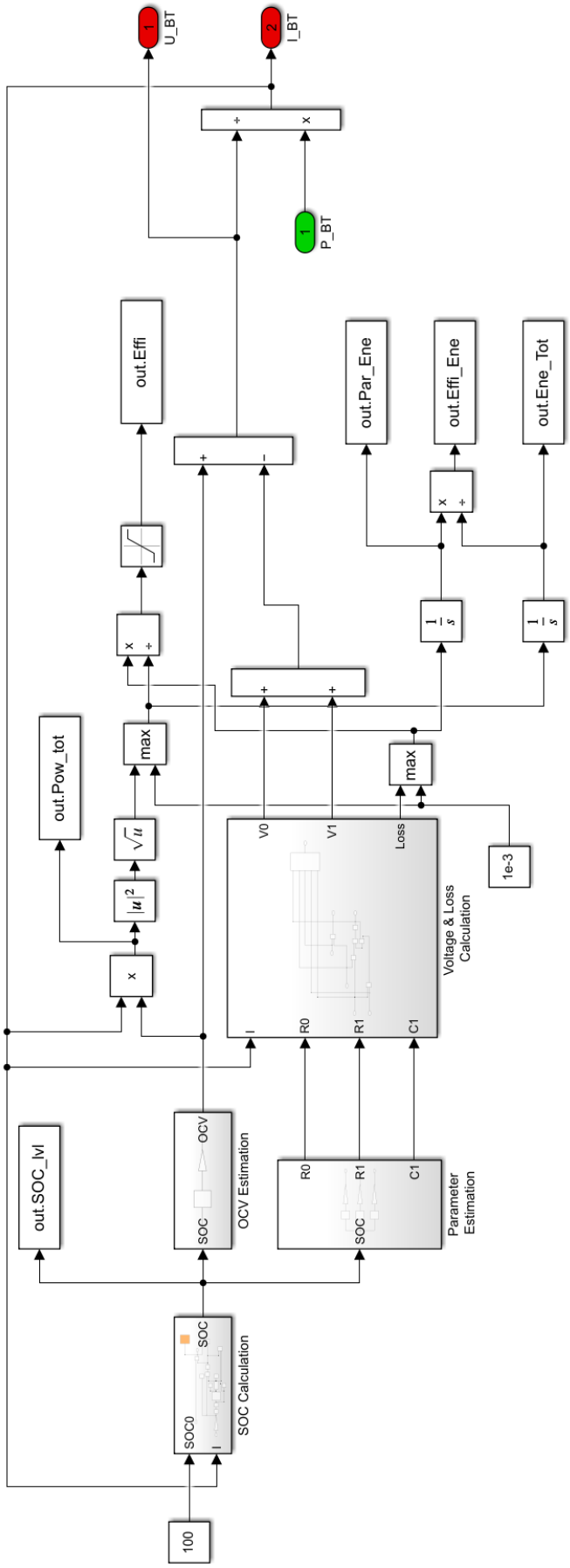

Figure A.1: Overview of the Simulink model of the voltage model

Table A.13: Emissions during cycling for the Swedish energy mix

	35[μm]	50[μm]	66.2[μm]	80[μm]	95[μm]
NMC-811[g CO_2eq/km]	7.3484	7.2887	7.3245	7.5029	7.7323
NMC-111 [g CO_2eq/km]	7.5561	7.4053	7.3716	7.4469	7.6009
LFP [g CO_2eq/km]	7.7631	7.7867	7.8159	7.9819	8.3441

Table A.14: Emissions contributed to losses during cycling for the Swedish energy mix

	35[μm]	50[μm]	66.2[μm]	80[μm]	95[μm]
NMC-811 [mg CO_2eq/km]	155.2	204.7	287.7	391.6]	477.9
NMC-111 [mg CO_2eq/km]	141.6	163.8	211.8	290.8	407.4
LFP [mg CO_2eq/km]	72.7	141.1	242.4]	364.9	508.7

Table A.15: Emissions during cycling for the South Korean energy mix

	35[μm]	50[μm]	66.2[μm]	80[μm]	95[μm]
NMC-811 [g CO_2eq/km]	126.76	125.73	126.35	129.42	133.38
NMC-111 [g CO_2eq/km]	130.34	127.74	127.16	128.46	131.12
LFP [g CO_2eq/km]	133.91	134.32	134.82	137.69	143.94

Table A.16: Emissions contributed to losses during cycling for the South Korean energy mix

	35[μm]	50[μm]	66.2[μm]	80[μm]	95[μm]
NMC-811 [g CO_2eq/km]	2.6764	3.5317	4.9630	6.7549	8.2433
NMC-111 [g CO_2eq/km]	2.4429	2.8257	3.6531	5.0166	7.0268
LFP [g CO_2eq/km]	1.2544	2.4332	4.1812	6.2939	8.7745

DEPARTMENT OF POWER ELECTRIC ENGINEERING
CHALMERS UNIVERSITY OF TECHNOLOGY
Gothenburg, Sweden
www.chalmers.se

CHALMERS
UNIVERSITY OF TECHNOLOGY